# Comparing Galaxy Morphology at Ultraviolet and Optical Wavelengths

L. E. Kuchinski[1], W. L. Freedman[2], Barry F. Madore[1,2], M. Trewhella[1], R. C. Bohlin[3], R. H. Cornett[4], M. N. Fanelli[4,5], P. M. Marcum[6], S. G. Neff[7], R. W. O'Connell[8], M. S. Roberts[9], A. M. Smith[7], T. P. Stecher[7], W. H. Waller[4,10]

## ABSTRACT

We have undertaken an imaging survey of 34 nearby galaxies in far–ultraviolet (FUV, $\sim 1500\AA$) and optical ($UBVRI$) passbands to characterize galaxy morphology as a function of wavelength. This sample, which includes a range of classical Hubble types from elliptical to irregular with emphasis on spirals at low inclination angle, provides a valuable database for comparison with images of high–$z$ galaxies whose FUV light is redshifted into the optical and near–infrared bands. Ultraviolet data are from the UIT *Astro–2* mission. We present images and surface brightness profiles for each galaxy, and we discuss the wavelength–dependence of morphology for different Hubble types in the context of understanding high–$z$ objects. In general, the dominance of young stars in the FUV produces the patchy appearance of a morphological type later than that inferred from optical images. Prominent rings and circumnuclear star formation regions are clearly evident in FUV images of spirals, while bulges, bars, and old, red stellar disks are faint to invisible at these short wavelengths. However, the magnitude of the change in apparent morphology ranges from dramatic in early–type spirals with prominent optical bulges to slight in late–type spirals and irregulars, in which young stars dominate both the UV and optical emission. Starburst galaxies with centrally concentrated, symmetric bursts display an apparent "E/S0" structure in the FUV, while starbursts associated with rings or mergers produce a peculiar morphology. We briefly discuss the inadequacy of the optically–defined Hubble sequence to describe FUV galaxy images and estimate morphological $k$–corrections, and we suggest some directions for future research with this dataset.

[1]Infrared Processing and Analysis Center, Caltech/JPL, Pasadena, CA 91125
[2]Observatories of the Carnegie Institution of Washington, Pasadena, CA 91101
[3]Space Telescope Science Institute, Baltimore, MD 21218
[4]Raytheon ITSS Corp., NASA Goddard Space Flight Center, Greenbelt, MD 20771
[5]Department of Physics, University of North Texas, Denton, TX 76023
[6]Department of Physics, Texas Christian University, Fort Worth, TX 76129
[7]Laboratory for Astronomy and Solar Physics, NASA Goddard Space Flight Center, Greenbelt, MD 20771
[8]Department of Astronomy, University of Virginia, Charlottesville, VA 22903
[9]National Radio Astronomy Observatory, Charlottesville, VA 22903
[10]Department of Physics and Astronomy, Tufts University, Medford, MA 02155

## 1. Introduction

An understanding of the ultraviolet (UV) properties of local galaxies is essential for interpreting images of high–redshift systems and especially critical in searches for morphological evolution in the galaxy population. At redshifts of $z \sim 3 - 10$, the rest–frame UV light of galaxies is shifted into the optical (1500Å observed in $V$–band at $z \sim 2.7$) and near–infrared (1500Å observed in $H$–band at $z \sim 10$) regions of the spectrum that are easily observable from the ground. Although one operational approach to overcoming this "band–shifting" problem is to observe in the infrared (*e.g.* Teplitz et al. 1998), the rate of data acquisition for galaxy images is generally highest at optical wavelengths where detectors are larger and the sky background is lower than in the infrared. Under these circumstances, the most direct method to compare present–day galaxies to those in the early universe is to build a large sample of local UV galaxy data.

Recent deep surveys suggest that galaxies with peculiar morphology are more prevalent at high redshift (*e.g.* Brinchmann et al. 1998; Abraham et al. 1996). However, it is difficult to quantify the influence of band–shifting on observed differences between the optical characteristics of nearby galaxies and the rest–frame UV appearance of distant ones because UV and optical morphology are not often well–coupled (O'Connell 1997a; Marcum et al. 1997, 2000). Rest-frame UV images of galaxies often suggest a later Hubble type than the corresponding optical appearance: bulges are less prominent, galaxy light appears more patchy, and in extreme cases the different star–forming regions in a single galaxy may appear as separate systems in the UV (O'Connell 1997a; O'Connell & Marcum 1996). On the other hand, recent deep NICMOS imaging of distant galaxies at longer rest wavelengths suggests that some of the morphological peculiarities are still visible in the optical and thus are intrinsic in the galaxies' structure (*e.g.* Bunker 1999; Teplitz et al. 1998). Although methods exist to estimate UV morphology by extrapolation from optical data (Abraham 1998; Abraham, Freedman, & Madore 1997), they rely on the use of global galaxy spectral energy distributions that may not accurately represent localized conditions, especially in dusty or starbursting regions. For example, Donas, Milliard, & Laget (1995) find a variation among UV$-b$ colors in galaxies with identical $b - r$. The availability of FUV images for bright, well–resolved galaxies of a range of Hubble types would facilitate a more direct comparison between local and distant galaxy populations.

The appearance of galaxies in the UV is determined primarily by emission from hot stars and by the distribution of dust, with a contribution in the central regions from an AGN if one is present and unobscured. Light in the ∼1500Å far–ultraviolet (FUV) band of the Ultraviolet Imaging Telescope (UIT, Stecher et al. 1997) originates in young objects of spectral types O and B (Fanelli et al. 1997) and, if old populations are present, in certain types of low–mass stars in late stages of evolution (the "UVX" population, see O'Connell 1999 for a review). Thus this region of the spectrum can probe timescales of young stellar populations between that studied via $H\alpha$ emission (only O stars, ∼ 5 Myr) and that evident in the optical colors (which trace the age of a stellar population on timescales of a few Gyr; O'Connell 1997b) .

Opacity due to dust in the FUV is a factor of ∼2.5 higher than in the optical $V$ band, assuming a Galactic extinction law (Cardelli, Clayton, & Mathis 1989), and even larger for Small Magellanic Cloud–type dust (Gordon, Calzetti, & Witt 1997). The young, massive stars that provide the bulk of the UV emission also tend to have small scale heights, less than or similar to that of the dust, while older stars that dominate at optical wavelengths and have scale heights greater than that of the dust layer (Mihalas & Binney 1981). The degree to which dust extinguishes the UV light of highly inclined disk galaxies is unclear. It likely depends strongly on the relative geometry of star–forming regions and dust concentrations, a phenomenon recently noted in optical/NIR studies of nearby galaxies as well as in theoretical studies of systems with a mixture of stars and dust (Kuchinski et al. 1998; Gordon et al. 1997; Huizinga 1995). For instance, NGC 4631 is quite bright in the FUV and blue in FUV–optical colors, and it does not show evidence for strong attenuation (Smith et al. 1997, 2000; O'Connell 1997a). However, NGC 891 is only barely detected (Marcum et al 1997, 2000), a phenomenon that Smith et al. suggest is due to extinction effects. UV morphology may also be dramatically influenced by specific features such as dust lanes, as noted in Cen A by O'Connell (1997a). Scattering by dust grains is quite efficient in the FUV (Witt et al. 1992) and may contribute significantly to the emission near H II regions and in spiral arms (Waller et al. 1997a; Stecher et al. 1982).

Prior to the Space Shuttle–borne UIT *Astro* missions, UV imaging of galaxies was limited to low resolution and/or small fields of view (see Brosch 1999 for a detailed review). UIT–prototype rocket–borne experiments in the 1980's provided images of five nearby galaxies with a resolution of $\sim 15''$ and ten more with a resolution of $100''$ (Hill, Bohlin, & Stecher 1984; Bohlin et al. 1991). The FOCA balloon experiment yielded images of similar resolution for six nearby galaxies (Blecha et al. 1990). Recently, higher resolution UV images of 110 galaxy nuclei (Maoz et al. 1996) and nine starburst galaxies (Meurer et al. 1995) have been obtained at 2200$\AA$ using the Hubble Space Telescope's Faint Object Camera with a very small ($22''$) field of view. A FUV ($\sim$1500$\AA$) survey of galaxies at redshifts of $\sim$ 0.1–0.2 is also underway using the Space Telescope Imaging Spectrograph, again with a small ($25''$) field of view (Gardner et al. 1997). With a $40'$ field of view and $\sim 3''$ resolution, UIT was optimally suited to study the morphology of nearby galaxies with good resolution. The usefulness of UV and optical images and radial profiles to study morphology variations with wavelength was demonstrated by Cornett et al. (1994) with UIT *Astro–1* data for M74, by Hill et al. (1997) for M51, and by Reichen et al. (1994) for M81.

In this and a companion paper (Marcum et al. 2000), we present the results of an UV–optical imaging survey of nearby bright galaxies. The UV images were obtained by the UIT during the *Astro–1* and *Astro–2* Spacelab missions in 1990 and 1995 respectively. Ground–based optical CCD images of the sample galaxies were obtained with pixel scales and fields of view approximately comparable to those of the UIT images. The *Astro–1* data presented in Marcum et al. include both FUV ($\sim$1500$\AA$) and NUV($\sim$2500$\AA$) data as well as optical images for 43 galaxies. This paper includes FUV and optical data for 34 galaxies observed during *Astro–2* with Hubble types specifically chosen to span the range E to Irr, including some interacting/merging systems. There is some emphasis in the sample selection on face–on spirals in which spiral arm, bar, and ring morphologies are easily observed. In Section 2 we discuss the sample selection, describe the UIT and optical observations, and explain the basic data reduction. Section 3 contains details of the registration of FUV and optical images and the extraction of surface brightness and color profiles. A qualitative comparison of UV and optical morphology, based on the images and profiles, is presented in Section 4. In Section 5 we provide a brief summary and discuss avenues of future investigation, including studies of the morphological $k$–correction and analysis of the star–formation histories of individual galaxies. In a subsequent paper (Kuchinski et al. 2000), we will investigate the quantitative concentration and asymmetry indices for these galaxies and consider the implications of these results for the study of high–redshift galaxies.

## 2. Observations and Data Reduction

### 2.1. Sample Selection

Our sample consists of 34 galaxies observed with UIT during the *Astro–2* mission for which we have also obtained ground–based optical images. Many of the galaxies were selected as part of a UIT Guest Observer program specifically to investigate the UV morphology in prototypes of different Hubble types. Others were observed during UIT studies of starburst galaxies (*e.g.* Smith et al. 1996), early–type galaxies (Ohl et al. 1998), AGNs (Fanelli et al. 1997a), or individually for selected purposes. It is important to remember that while this sample does contain galaxies with a range of morphologies, it was not chosen to statistically represent the relative distribution of Hubble types in the local population. The galaxies have types E to Irr ($T$ = –5.0 – +10.0), and are located at distances of $\sim 2 - 25$ Mpc ($H_0$ = 75km/s/Mpc). Late–type systems in which star formation produces prominent morphological features in the FUV are emphasized. Three sets of interacting pairs are included: NGC 3226/7, NGC 4038/9, and NGC 5194/5. Table 1 gives basic properties of the sample galaxies.

### 2.2. Ultraviolet Observations and Data Reduction

The sample galaxies were observed in the FUV with UIT, a 38cm. Ritchey–Chretien telescope mounted on the *Astro* payload. The *Astro–2* mission during which these data were obtained was flown on the Space Shuttle Endeavour on 2–18 March 1995. Details of the telescope and instrumentation, as well as specific information about pipeline data processing of the UV images, can be found in Stecher et al. (1997) and will be briefly summarized here. Only the FUV ($\sim$1500Å) camera was operational during the *Astro–2* mission. Two FUV filters were used: the B1 filter with an effective wavelength of 1520Å and width

354Å, and the slightly narrower B5 filter with effective wavelength of 1615Å and width 225Å, which was used during daylight observations to exclude dayglow emission lines (Hill et al. 1998; Waller et al. 1995). Based on observations of early–type galaxies (Ohl et al. 1998), there is no evidence for a "red leak" in the system. The camera consisted of a two–stage image intensifier coupled to Kodak IIa–0 film on which the images were recorded. The photographic film was digitized with a 20$\mu$m square aperture and 10$\mu$m sample spacing, then binned to a 20$\mu$m spacing (Stecher et al. 1997). In the pipeline data reductions, background "fog" from the photographic film was subtracted, and the images were linearized, flatfielded, and calibrated. The final output images have a scale of 1.136$''$/pixel and a typical point spread function of FWHM $\sim 3''$ in the central 16$'$ of the frame, in which nearly all of the galaxies studied here are imaged (Stecher et al. 1997). UIT images with enough stars to calculate astrometric solutions were corrected for distortion (Stecher et al. 1997; Greason et al. 1994); these data products were used where available. However, we note that even on uncorrected images, the uncertainty due to distortion in the central part of the frame (where most of our galaxy images are located) is less than or equal to the PSF FWHM.

After visual inspection of all available FUV images for each galaxy, we selected the ones with the best signal–to–noise and image quality for further analysis. In most cases this is the image with the longest exposure time, unless that image is noted in the UIT log to suffer pointing problems or other defects. In such cases, the longest exposure time image of good quality was used. The UV–bright center of NGC 4151 is saturated in the UIT *Astro–2* images; for photometry of this galaxy, see Fanelli et al. (1997a). We select a long–exposure UIT image of this galaxy to show the faint spiral arms as well as the active nucleus. The UIT exposure time of the image selected for each galaxy is given in Table 2.

Many of the FUV images required no further processing beyond the UIT pipeline, but some have a noticeable "stripe" artifact through the center of the frame (Stecher et al. 1997). If the entire galaxy was located within the stripe, no correction was made and care was taken to determine the sky value within the stripe as well. For galaxies located partly within and partly outside the stripe, a quadratic surface was fit to the frame after masking out the central region (where the galaxy lies) and the frame edges. This surface was then subtracted before the sky background and surface brightness profile were measured. The FUV sky background is typically low (see Waller et al. 1995 for a discussion of the UV background), ranging from undetectable (with a 1–$\sigma$ limit of $\sim$25 mag arcsec$^{-2}$) up to 22 mag arcsec$^{-2}$ for a few images acquired during daylight.

### 2.3. Optical Observations and Data Reduction

Broad–band optical images of the sample galaxies were obtained over the past several years with the Las Campanas Observatory 2.5m du Pont telescope, the CTIO 1.5m telescope, and the Palomar 1.5m and 5m telescopes. All of the galaxies presented here were imaged in at least one of the $UBVR_cI_c$ bands; many have multi–color photometry. Observations at Las Campanas were carried out using the 2048$\times$2048 Tek 5 CCD with a scale of 0.26$''$/pixel. The CTIO observations utilized the Tek 2048$\times$2048 CCD with a scale of 0.43$''$/pixel. Data from the Palomar 1.5m telescope were taken using the 2048$\times$2048 CCD13 or CCD16 with a scale of 0.37$''$/pixel; some of these were binned to 1024$\times$1024 with a scale of 0.74$''$/pixel. Observations with the Palomar 5m telescope used the COSMIC camera with a 2048$\times$2048 CCD and a scale of 0.28$''$/pixel; again some images were binned to a scale of 0.55$''$/pixel. Table 2 shows the telescope, filters, and exposure times for each galaxy.

Data reduction for the optical images was carried out using the IRAF (Tody 1986) and VISTA (Stover 1988) packages. The images were bias–subtracted and flatfielded with twilight or dome flats for each filter. An apparent gradient in the background of some of the $V$, $R$, and $I$ frames taken at Palomar remained after these steps. A planar surface was fit to these frames after masking out the galaxy, then subtracted before further processing. Cosmic rays were identified with the IRAF "cosmicrays" package and were replaced with an average of surrounding pixel values. If more than one data frame was available for a galaxy in a specific filter, the frames were registered using the coordinates of several bright stars, scaled to the same exposure time, and a zeropoint offset was applied to match the background levels. The frames were then averaged (for two) or median combined (for three or more). Some of the images are saturated at the galaxy centers; no correction is applied but the saturated pixels were flagged for future consideration. Sky levels were determined in boxes away from the galaxy. In some cases (flagged in Table 2) the galaxy nearly fills the frame and thus the background level is somewhat uncertain. On images in which several regions of sky away from the galaxy can be measured, the typical r.m.s. scatter in sky levels across the frame is less than 2% of the sky value.

### 2.4. Data Calibration

Calibrations were applied to each image to obtain the approximate relative alignment of the multicolor light profiles presented in Section 3. The UIT data were calibrated using standard stars measured by the International Ultraviolet Explorer (*IUE*). The resulting flux calibration is estimated to be accurate to $\sim$ 15% (Stecher et al. 1997); this value includes the uncertainty in the final *IUE* calibration. Magnitudes are on the monochromatic system:

$$\mathrm{mag}_{\lambda} = -2.5\log_{10}(f_{\lambda}) - 21.1 \tag{1}$$

where the flux is in units of erg cm$^{-2}$s$^{-1}$ $\AA^{-1}$. Calibration data for each image are stored in the image headers of the UIT data products.

Because many of the optical data were obtained under non–photometric conditions, the frames were calibrated via comparison to published aperture photometry for each galaxy. We used the catalog of Prugniel & Heraudeau (1998), excluding any data whose zeropoint was found by these authors to be systematically offset by more than 0.05 mag. from that galaxy's curve of growth. We calculated the difference between a synthetic aperture magnitude measured on our galaxy image and the published value for each of the tabulated apertures that fit on our frame. After examining the residuals as a function of $(B-V)$ or $(V-I)$ color for those galaxies with sufficient published data over a range of colors, we found no strong evidence for color terms in the calibration. Therefore, we simply used the mean difference between the measured and published magnitudes as a calibration constant. For images in which the galaxy center was saturated, we compared the observed and published magnitudes in annuli between the smallest published aperture that enclosed all the saturated pixels and subsequent apertures. The typical scatter around this mean difference ranges from 0.02–0.15 mag., which is not unexpected for a mix of photometric and non–photometric data from several different instruments. The uncertainty in optical aperture magnitudes due to sky and instrument noise is typically $\leq 3\%$. If no catalog data were available for a particular galaxy/filter, we substituted an average of the calibration constants determined in that filter for other galaxies observed during the same night. As all but one of these cases involved calibration of $R$ or $I$–band data, airmass differences between the galaxies that were bootstrapped and those for which calibrations were determined from the literature are likely to contribute only small errors. Galaxies for which this procedure was necessary are flagged in Table 2; their calibrations are correspondingly less certain than the others. Overall, combining the noise and calibration errors, we estimate an uncertainty in the optical magnitudes of $\leq 15\%$, with the exact value for each galaxy depending on the quality of the observations and the availability of published data.

### 2.5. Image Alignment and Stellar Masks

In order to facilitate the direct comparison of galaxy morphology at UV and optical wavelengths, we transformed the coordinates of the optical data onto the system of the UIT data and smoothed all data for a particular galaxy to the same resolution. Because the FUV images contain few or no stars, the coordinates of UV–bright star–forming regions were used to determine a linear transformation (rotation, scaling, and translation) between the shortest wavelength optical image and the UIT data. After the transformation was applied to that optical image, the centroids of several bright stars were used to align additional optical data. Finally, we measured the FWHM of the point spread function (PSF) on each optical image and smoothed the frame to the UIT resolution of $3''$. The PSF FWHM for two galaxies, M51 and NGC 925, were slightly larger than the UIT FWHM ($4''$ and $4.5''$ respectively); in these cases the UIT images were smoothed to the optical resolution. The final images have the UIT scale of $1.136''$/pixel, implying physical scales ranging from $\sim 10 - 140$ pc/pixel for our sample galaxies.

Foreground stars and any remaining artifacts were masked out on the optical and FUV data before producing the images and surface brightness profiles presented in Section 3. For the optical data, we identified stars on the longest wavelength image and created a mask that was used to interpolate over those pixels on all of the optical images. Most of the sample galaxies lie at high Galactic latitude, so few foreground bright stars were present. However, in the case of NGC 2403, badly saturated bright stars in the $R$ and $I$–bands necessitated masking large areas of those images. For this galaxy, we created a separate mask for the $UBV$ images, which did not require such extensive corrections. In a few cases it was difficult to determine whether bright spots within the galaxy were foreground stars or HII regions; here we carefully compared the optical and FUV images and masked only those spots that were not visible in the FUV. Some galaxies also required a FUV mask to interpolate over small, bright point–like or streak artifacts (mostly due to cosmic rays) that remained after prior data processing.

## 3. Images and Surface Brightness Profiles

In Figures $1(a-n)$, we present multiwavelength images for the sample galaxies. The sky backgrounds have been removed, foreground stars have been masked as described above. For display purposes only, image pixel values have been converted to "calibrated" flux units such that:

$$\mathrm{mag\ arcsec}^{-2} = 26. - 2.5\log_{10}(\mathrm{pixel\ value}) \quad (2)$$

The images for a given galaxy are displayed using the same range of calibrated brightness for each filter, so that pixels with the same brightness (flux/$\AA$) have a constant gray level on each image. This mode of presentation shows the relative limiting surface brightnesses of the data at different wavelengths. To conserve space, we do not show every optical image, as those from adjacent optical filters often look nearly identical. It is quite difficult to simultaneously show structure in the bright centers of galaxies and faint outlying features, so we present additional images of some galaxies with different scales or normalizations in Figures 2 and 3. The four FUV–bright galaxies shown in Figure 2 are displayed with a much larger scale to show the central regions. In Figure 3, we show several galaxies with red FUV–optical colors, mainly early–type galaxies or those with a prominent optical bulge. Here we show the optical images with a much larger stretch than the FUV data, so that the central structure of the optical image can be compared to the FUV. We also plan to make our images available to the community in digital form via the NASA/IPAC Extragalactic Database (NED); they can then be renormalized as appropriate for any application.

We extract surface brightness profiles for each galaxy by azimuthally averaging around concentric ellipses. The ellipse center, ellipticity, and position angle (P.A.) for each galaxy were determined by running an ellipse–fitting package in VISTA (based on the method of Kent 1983) on the longest available wavelength image, usually $R$ or $I$. The centroid was determined in a small box around the visual center of the galaxy, taking care to use an image in which the center was not saturated. The ellipticity and P.A. are determined from the outer ellipses, where their values were typically stable over a large range in radii. These ellipse parameters were used to obtain surface brightness profiles at all wavelengths, in order to avoid problems with determining centroids and fitting ellipses on the often asymmetric and irregular FUV images. For one galaxy, NGC 3115, we were unable to align the optical and FUV images due to a lack of bright features or foreground stars in the FUV. We determined a separate FUV ellipticity and P.A. for this galaxy using the ellipse fitting routine. The ellipticity and P.A. for each galaxy, which are given in Table 1, are quite similar to the $RC3$ (de Vaucouleurs et al. 1991) values ($\Delta\epsilon \sim 0.05$ and $\Delta$P.A. $\leq 15°$). The surface brightness profiles derived for each sample galaxy are shown in Figure $4(a-g)$, with data from the various filters denoted by different symbols. Images in which the galaxy center was saturated are identifiable by their flat profiles in the central regions; this is the case for several optical images and the inner $\sim 10''$ of the FUV data for NGC 4151. Profiles for a subset of our sample were compared to those extracted by Fanelli et al. (1997b) from the same data; no significant differences are noted. The profiles have not been corrected for foreground Galactic extinction. However, the foreground $A_B$ values (given in Table 1) are generally small, so even FUV extinctions of $\sim 2 \times A_B$ amount to $\leq 0.5$mag and would have little effect on the plots of Figure 4.

Three systems in our sample are interacting pairs for which it is difficult to separate the light profiles of the two galaxies: NGC 4038/9, NGC 3226/7, and NGC 5194/5 (M51a,b). (NGC 4647 and NGC 4649 are a close pair that may be undergoing a mild interaction, but their FUV isophotes do not overlap in our images.) For NGC 5194/5, the companion galaxy NGC 5195 is undetected in the FUV image and thus is not analyzed separately. The ellipse parameters for NGC 5194 are determined from a region unaffected by the companion on the optical images. Many of the outer ellipses cut through the companion, creating a slight "bump" in the outer part of the optical surface brightness profiles. The outer ellipses for NGC 3227 encompass all of the FUV light and a significant fraction of the optical light of its companion NGC 3226. Within the available software packages, it is impossible to avoid this situation without either severely truncating the NGC 3227 profile or changing the ellipticity so much that it no longer accurately reflects the shape of NGC 3227. However, the NGC 3226 profile of the region with detectable FUV emission is relatively unaffected. The merger system NGC 4038/9 is treated as one galaxy, as the FUV image does not suggest a simple division into two separate disks. We created an image of this system consisting of only pixels with flux greater than $1.5\sigma_{\rm sky}$ above the background that also have at least 4 adjacent pixels above the threshold. ("Adjacent" pixels are defined as those that share either an edge or corner with the pixel in question; thus each pixel has 8 adjacent neighbors.) This image is approximately circular, so we defined an aperture center at the geometric center of the FUV image and used circular annuli to measure the light profiles.

Color profiles are produced by subtracting the surface brightness profiles (in mag arcsec$^{-2}$) of different filters. The use of a single set of ellipse parameters for all images of a particular galaxy ensures that the light profiles at each wavelength sample the same physical region and thus can be compared in this simple manner. Color profiles for many of the sample galaxies will be presented and discussed in the next section.

## 4. Optical and FUV Morphology

In this section we present a qualitative discussion of the differences in apparent morphology between FUV and optical images. The morphological types included in each subsection below are approximate, stemming in part from the fact that several galaxies have characteristics associated with more than one "type". Rather than discussing each galaxy individually (as is done in Marcum et al. 2000), we summarize the changes in apparent morphology with wavelength for various Hubble types. (Interested readers can see the results for each individual galaxy from the data presented in Figure 1.) Throughout this section, we also consider implications of our analysis for the study of high–redshift galaxies that are observed in their rest–frame UV. It is important to remember that this level of discussion assumes no evolution of the star–formation rate: we simply consider what galaxies *identical* to local ellipticals, spirals, and irregulars would look like at high redshift. Galaxies undergoing their initial starburst or a subsequent period of increased star formation activity due to mergers, etc. would, of course, look different from the quiescent ellipticals and "normal" spirals in this sample and may more closely resemble star–forming irregular or peculiar systems.

### 4.1. Elliptical and S0 Galaxies

The elliptical and S0 galaxies in our sample feature smooth, compact FUV emission centered on the nuclear regions (see also the detailed analysis of UIT data for E/S0 galaxies in Ohl et al. 1998). In galaxies of this type, FUV emission is produced not by young stars but by the hot, evolved population responsible for the spectrosopic UV upturn (O'Connell 1999). The FUV light profiles of these systems – NGC 3379, NGC 3384, NGC 4649, NGC 3226, and NGC 3115 – drop off much more rapidly than the optical light, and the colors throughout are quite red (FUV–$R \sim$ 2–5). FUV half–light radii for these galaxies are ∼20–35% of their $B$–band values tabulated in the *RC*3 (we cannot compare directly to our optical data because most of the E/SO optical images suffer saturation in the center). The only exception to this pattern is NGC 1510, the interacting companion of NGC 1512. The FUV emission in this galaxy is comparable to the optical light in both brightness and physical extent and is likely due to tidally induced star formation rather than the evolved population. Although it is classified in the *RC*3 as a peculiar S0 galaxy, Sandage & Brucato (1979) classify NGC 1510 as an Amorphous galaxy, and it is also noted to be a star–forming blue compact dwarf (BCD) in Kinney et al. (1993) and an HII galaxy in NED. (The other S0/Amorphous galaxy in our sample, NGC 5195, is also interacting with companion galaxy NGC 5194 but is not detected in the FUV.)

It is difficult to predict the appearance of high–redshift E/S0 galaxies in their rest–frame FUV because the present–day UV emission mechanism, that of evolved stars, is likely to be weak to nonexistent at redshifts approaching $z \sim 1$ (Brown et al. 1998, 2000). Indeed, the UV upturn phenomenon is a potentially sensitive age indicator for evolved stellar populations, and thus its evolution with redshift could help identify the formation epoch of early–type galaxies (Yi et al. 1999). At high redshifts ellipticals may be undergoing an initial starburst and/or the UV upturn population will not yet have had time to evolve. In this case, the progenitors of present–day elliptical and S0 galaxies may look like local starbursts or mergers depending on their formation mechanism and the timing of the observations. However, if some high–redshift E/S0's were quiescent and identical to local early–type galaxies (*i.e.* assuming a very high formation redshift), they would still have the smooth and symmetric light distributions associated with early types. Their FUV emission would be much more compact than the optical light, which would lead to difficulties in detection and confusion in estimating their typical size.

### 4.2. Early–Type Spiral Galaxies

Galaxies of Hubble type Sa–Sbc tend to appear as later–type spirals in the FUV than at optical wavelengths, primarily due to fading of the red bulge and bar in UV images. A significant fraction of the FUV light in these systems comes from star–forming regions in the spiral arms, which are visible in the images of Figure 1 and appear as "bumps" in the FUV surface brightness profiles of Figure 4 (see also Fanelli et al. 1997b). Some early–type spirals, such as M63 and NGC 1672, also appear more patchy or fragmented in the FUV because old stars in the underlying smooth disk do not produce much light at very short wavelengths. These results are in agreement with earlier work by O'Connell (1997a) and O'Connell & Marcum (1996) for smaller samples of galaxies. The dramatic fading of light in the central regions (also noted by O'Connell 1997a and Waller et al. 1997b) produces a global pattern in which the central FUV–optical colors are much redder than the outer regions, as shown in Figure 5 for M 51, NGC 1566, and M 63. Two notable exceptions to this pattern are NGC 4151, in which the Seyfert 1 nucleus dominates the central FUV emission and is much brighter than the weak spiral arms, and NGC 1068, in which the FUV–bright Seyfert 2 nucleus and surrounding star–formation combine to produce a very blue center. The UV morphologies and luminosities of the AGN and star–forming components in these two galaxies are discussed in more detail by Fanelli et al. (1997a).

Many early–type spirals also show evidence of star–forming inner rings or circumnuclear star formation, which often dominate the FUV images and light profiles. Images of these features, which are present in NGC 1097, NGC 1512, NGC 1672, NGC 3310, NGC 3351, and NGC 4736, are shown in Figure 6, and the associated color profiles are plotted in Figure 7. The star–forming rings appear as spikes of FUV brightness or very blue color in the radial profiles of Figures 4 and 7. Inner and circumnuclear rings are thought to be orchestrated by dynamical resonances, which are often associated with central bars (*e.g.* Storchi–Bergmann, Wilson, & Baldwin 1996; Buta & Combes 1996). The FUV properties of some specific ringed galaxies are discussed by Waller et al. (1997c, 2000) for NGC 4736, Smith et al. (1996) for NGC 3310, and Marcum et al. (2000).

Galaxies classified from their optical images as early–type spirals may present a variety of different appearances when viewed at high redshift, in their rest–frame FUV. Optically barred galaxies such as NGC 1097 and NGC 1365 will appear unbarred in the ultraviolet. Isolated galaxies such as NGC 1672 that appear highly fragmented in the FUV may be mistaken for an ongoing merger. Images of distant systems may recover only the FUV–bright star–forming rings or circumnuclear star formation, yielding little evidence of the underlying regular structure seen in the galaxy's optical light (see also Waller et al. 1997b). On the other hand, galaxies such as NGC 4151 appear to have an earlier morphological type in the FUV due to the prominence of highly symmetric and strongly peaked emission from the active nucleus. Finally, the appearance of a galaxy undergoing a global starburst, such as NGC 3310, does not differ a great deal between the FUV and optical because the light at both wavelengths is dominated by young stars. We have found that all of these effects can vary in magnitude, such that some galaxies would be assigned nearly the same Hubble type in the optical and FUV, while others would have very different classifications. Overall, most optically–classified early–type spirals present the appearance of a later type in the FUV, but a small fraction may appear to have identical or earlier FUV types in the presence of starburst activity or an AGN.

### 4.3. Late–Type Spirals, Irregulars, and Starbursts

Galaxies that are optically classified as late–type spirals generally do not show as dramatic a difference between their FUV and optical morphologies as do early–type spirals. Although they often appear somewhat more patchy in the FUV, there is no prominent optical bulge whose absence at short wavelengths is noticeable. Star formation occurs over a large fraction of the galaxy, producing both FUV and optical light in the same physical regions. A number of these galaxies, including NGC 4449, NGC 925, NGC 1313, and IC 2574, show color profiles that have no definite trend with radius. These profiles, examples of which are displayed in Figure 8, are either flat or bumpy depending on the relative prominence of star–forming regions against the background disk. Figure 9 shows color profiles for the central starburst galaxies M83, NGC 4214, and NGC 5253, which are bluest in their centers. NGC 4214 and NGC 5253 have global color gradients in the opposite direction of that observed in early–type spirals due to the presence of a blue starburst superposed on a more extended old stellar distribution. This "starburst core" morphology has been previously noted in FUV–optical image comparisons of NGC 4214 (Fanelli et al. 1997c) and NGC 5253 (Kinney et al. 1993). A central starburst combined with bright star–forming regions in the outer disk can also produce a flat color profile, which is the case for NGC 2903 (also shown in Figure 9).

We find that the morphological $k$–correction for late–type galaxies is expected to be highly dependent on whether or not they host starburst activity. As evident from their similar FUV and optical morphology, non–starbursting late–type galaxies (dominated by ongoing disk star formation) viewed at high redshift would not generally appear to have a very different type from their local counterparts. Increased patchiness in the FUV (if it were still detectable at large distances) might suggest a slightly later type than the optical appearance. However, galaxies with central starbursts like those seen in NGC 4214 and NGC 5253 might present compact cores surrounded by diffuse light, similar to some objects seen on deep HST images (Giavalisco, Steidel, & Duccio Macchetto 1996a). The symmetric central burst in NGC 5253 might even appear to be an E or S0 galaxy in the absence of the old stars. If starburst systems are more prevalent at high redshift, their strong influence on the rest–frame UV morphology must be considered when studying the evolution of the galaxy population.

### 4.4. Interacting Systems

As might be expected, the morphological $k$–correction for interacting galaxies depends strongly on the details of the interaction itself. Three objects in our sample are currently undergoing interactions of various degrees: NGC 4038/9 (the Antennae), NGC 3226/7, and NGC 5194/5 (M51). The merger of two disk galaxies in NGC 4038/9 has produced a significant amount of massive star formation, concentrated mainly between the two disks and around the edge of the NGC 4038 disk. Thus the FUV image shows a partial outline of the merger system, and, without the corresponding optical data, suggests the appearance of a single, drastically perturbed galaxy. However, the old populations visible in long–wavelength optical images clearly delineate the inner disks and tidal tails that identify NGC 4038/9 as an ongoing disk–disk merger. In spite of the dramatic difference between its FUV and optical appearances, NGC 4038/9 is clearly peculiar at both wavelengths and thus would not be misclassified as any sort of "normal" Hubble type galaxy when viewed at high redshift. Both galaxies in the NGC 3226/7 interacting pair present FUV morphologies consistent with what would be expected from their Hubble types: the elliptical NGC 3226 appears highly concentrated and the Sa NGC 3227 shows emission from the center and a few faint disk star–formation regions. In this case, the influence of the interaction in determining the FUV morphology is confined to its possible role in driving the Seyfert nucleus and circumnuclear star formation in NGC 3227 (Keel 1996; Gonzalez Delgado & Perez 1997). NGC 5195 is not detected in the FUV, likely due to obscuration by dust from a foreground spiral arm in NGC 5194 as well as possible internal extinction (see Sandage 1961. Barth et al. (1998) also suspect that dust is responsible for their failure to detect NGC 5195 at 2200Å.) Observed at high redshift in its rest–frame UV, the M51 double–galaxy system would appear to be an isolated spiral galaxy. Although the examples discussed above demonstrate the difficulty of relating UV and optical morphology for interacting systems, interactions that are significant enough to severely distort the galaxies involved are often associated with enhanced star formation rates that may identify the system as "abnormal" in the FUV as well (Kennicutt 1998 and references therein).

### 4.5. Dust and Morphology

Throughout this section we have discussed FUV morphology mainly in terms of the current star formation, but, as suggested by the example of M51, one cannot neglect the possibility that extinction also influences the UV appearance of galaxies. It is difficult to ascertain whether the "patchiness" or fragmented appearance of many galaxies in the FUV is due to internal extinction or to the pattern of massive star formation. Two of the most highly inclined ($i \sim 65°$)

galaxies in our sample, NGC 2841 and NGC 2903, have asymmetric FUV emission with the bright side corresponding to what appears to be the unobscured side of the optical disk. On the other hand, NGC 2403 and IC 2574 also have $i \geq 60°$ but do not appear to suffer heavy extinction on one side of the disk. These results provide further confirmation of the variations in FUV brightness of edge–on galaxies noted by Smith et al. (1997, 2000) for NGC 4631 (FUV–bright) and NGC 891 (undetected). An extreme case of extinction effects was discussed above for NGC 5195 (M51b), which is completely obscured in the FUV by the foreground spiral arm of NGC 5194 (M51a). As noted in the introduction, the role of dust in determining the observed FUV morphology depends strongly on the dust–star geometry of individual galaxies and is thus difficult to predict from optical images alone.

## 5. Summary and Discussion

We have presented FUV and optical images and surface brightness profiles for 34 galaxies observed with the UIT and compared the apparent morphology at different wavelengths in the context of interpreting images of high–redshift objects. The UIT data represent the most detailed set of FUV images obtained to date for large, nearby galaxies that are well–resolved. Present–day elliptical and S0 galaxies appear smooth and symmetric in FUV as well as in optical images, but they are much more compact in the FUV and may be faint and/or unresolved at high redshift unless they are actively forming stars at that particular look–back time. The majority of spiral galaxies in our sample appear to have a later Hubble type in the FUV than at optical wavelengths due to increased patchiness in combination with the fading of light from the bulge and/or bar populations. This effect is particularly dramatic for the early–type spirals, in which bulges and often bars are prominent optical features. The optical and FUV morphologies of late–type spirals and irregular galaxies do not differ as much as the earlier types because young stars dominate the light in both spectral regimes. Some galaxies appear highly fragmented in the FUV images in spite of a regular optical morphology, making it hard to determine from UV data alone whether they are single systems or multiple mergers. Even assuming their current rates and patterns of star formation, many spirals viewed at high redshift would be assigned later Hubble types than their local counterparts due to the bandshifting effects. Central or circumnuclear starbursts and star–forming rings, and bright spiral arms dominate the FUV light and FUV–optical color profiles of many galaxies. Depending on the relative geometry of dust and young stars, extinction can play a varying role (small to dominant) in determining the apparent FUV morphology. From the galaxy sample presented here, it is apparent that understanding the correlation between FUV and optical morphology depends on one's knowledge of not only the global optical Hubble type but also of smaller scale features, mostly those due to recent star–formation patterns.

The fragmented appearance of many of the FUV images and the prominence of young stars in structures such as rings or fragments of spiral arms produces FUV morphologies that do not readily fit into the traditional bins of the Hubble sequence. In order to characterize rest–frame UV galaxy populations at both low and high redshift, it will be necessary to find new ways of describing the morphology that do not by default cause the majority of galaxies to fall into the "peculiar" or other catch–all bins. It would also be desirable to have an objective classification scheme to express the similarities or differences between local and distant galaxies in quantitative terms. However, UV data pose problems for many automated classification schemes because galaxy centers are often ill–defined and the patchy nature complicates the selection of an aperture that encloses a single system. Future work in this area will use UIT data to identify new features or indices that better describe the UV morphology of galaxies.

The dataset presented in this paper will be valuable for studying the morphological $k$–correction that must be taken into account when interpreting deep optical images such as the *Hubble Deep Field* (HDF, Williams et al. 1996). The dependence of FUV morphology on features that are considered minor or secondary details in the optical highlights the difficulty of studying evolution in the galaxy population by comparing rest–frame UV observations of high–redshift galaxies to the optical properties of local samples. The comparison between local and distant UV galaxy images is much more direct than relying on estimates of the UV morphology extrapolated from optical light and colors (*e.g.* Abraham et al. 1997). Indeed, a small sample of UIT galaxy images from the *Astro–1* mission have been used to simulate the appearance of high–redshift counterparts of nearby bright galaxies (Giavalisco et al. 1996b). In a subsequent paper (Kuchinski et al. 2000), we simulate the cosmological distance effects of surface brightness dimming and loss of spatial resolution on the FUV images of our larger *Astro–2* galaxy sample. These simulations provide examples of how local galaxies would appear in the HDF at redshifts of $\sim 1-4$. In that paper, we also attempt to quantify the effects of bandshifting and distance on morphology using simple parameters such as the central concentration and asymmetry of galaxies.

One of the primary goals of studying morphology is to infer the past or ongoing physical processes that have shaped galaxies. In combination with current knowledge about the dynamical states of nearby galaxies, our multi–wavelength dataset and future UV imaging data from the GALEX sky survey (Martin et al. 1997) could be used to relate UV morphology to physical structures or properties. For example, Waller et al. (1997b, 2000) find that UV–bright starburst rings likely result from dynamical resonances with a bar component. Thus ring features may predict the presence of an underlying disk and bar system even in UV images that appear to be fragmented or otherwise dynamically disorganized. It would also be of interest to further investigate the suggestion of Waller et al. (1997b) that optical Hubble type may be correlated with FUV–$V$ color (although rest–frame $V$–band data will not necessarily be available for high–redshift galaxies). If relations between UV morphology and physical properties can be found in local galaxies *and* shown to extend to large look–back times, they could provide a valuable tool for studying the distant universe through rest–frame UV imaging.

The authors gratefully acknowledge the help of R. Bernstein, J. Parker, R. Phelps, and N. Silbermann for obtaining some of the optical imaging data presented here. We thank O. Pevunova for assistance with preliminary data reduction. We are also grateful to the anonymous referee for many constructive suggestions. Funding for the UIT project was provided through the Spacelab office at NASA Headquarters under Project Number 440-51. WLF and BFM acknowledge support from the Astro–2 Guest Investigator Program through grant number NAG8–1051. Some of the data presented here were obtained at CTIO, which is operated by AURA as part of NOAO under a cooperative agreement with the National Science Foundation. This research has made use of the NASA/IPAC Extragalactic Database (NED), which is operated by the Jet Propulsion Laboratory, California Institute of Technology, under contract with NASA.

## REFERENCES

Abraham, R. 1998 in The Ultraviolet Universe at Low and High Redshift, ed. W. H. Waller et al. (Woodbury, NY: AIP), 195

Abraham, R. G., Freedman, W. L., & Madore, B. F. 1997, in *HST* and the High Redshift Universe, ed. N. R. Tanvir, A. Aragon–Salamanca, & J. V. Wall (Singapore: World Scientific), 57

Abraham, R. G., Tanvir, N. R., Santiago, B. X., Ellis, R. S., Glazebrook, K. G., & van den Bergh, S. 1996, MNRAS, 279, L47

Barth, A. J., Ho, L. C., Filippenko, A. V., & Sargent, W. L. W. 1998, ApJ, 496, 133

Blecha, A., Golay, M., Huguenin, D., Reichen, D., & Bersier, D. 1990, A&AS, 233, L9

Bohlin, R. C., et al. 1991, ApJ, 368, 12

Brinchmann, J., et al. 1998, ApJ, 499, 112

Brosch, N. 1999, Experimental Astronomy, 9, 119

Brown, T. M., Bowers, C. W., Kimble, R. A., & Ferguson, H. C. 2000, ApJ, 529, L89

Brown, T. M., Ferguson, H. C., Deharveng, J.–M., & Jedrzejewski, R. I. 1998, ApJ, 508, L139

Bunker, A. J. 1999, to appear in The OCIW Workshop on Photometric Redshifts, ed. Weymann, R., Storrie–Lombardi, L., Sawicki, M., & Brunner, R. (*astro-ph* 9907196)

Burstein, D., & Heiles, C. 1984, ApJS, 54, 33

Buta, R., & Combes, F. 1996, Fund. Cosmic Phys., 17, 95

Cardelli, J. A., Clayton, G. C., & Mathis, J. S. 1989, ApJ, 345, 245

Cornett, R. H., et al. 1994, ApJ, 426, 553

de Vaucouleurs, G., de Vaucouleurs, A., Corwin, H. G., Buta, R. J., Paturel, G., & Fouque, P. 1991, Third ReferenceCatalogue of Bright Galaxies, (New York: Springer Verlag) (*RC3*)

Donas, J., Milliard, B., & Laget, M. 1995, A&A, 303, 661

Fanelli, M. N., Collins, N., Bohlin, R. C., Neff, S. G., O'Connell, R. W., Roberts, M. S., Smith, A. M., & Stecher, T. P. 1997a, AJ, 114, 575

Fanelli, M. N., et al. 1997b, in The Ultraviolet Universe at Low and High Redshift, ed. W. H. Waller et al. (Woodbury, NY: AIP), 83

Fanelli, M. N., et al. 1997c, ApJ, 481, 735

Gardner, J. P., Heap, S. R., Malumuth, E. M., Hill, R. S., & Smith, E. P. 1997, in The Ultraviolet Universe at Low and High Redshift, ed. W. H. Waller et al. (Woodbury, NY: AIP), 429

Giavalisco, M., Livio, M., Bohlin, R. C., Duccio Macchetto, F., & Stecher, T. P. 1996b, AJ, 112, 369

Giavalisco, M., Steidel, C. C., & Duccio Macchetto, F. 1996, ApJ, 470, 189

Gonzalez Delgado, R. M., & Perez, E. 1997, MNRAS, 284, 931

Gordon, K. D., Calzetti, D., & Witt, A. N. 1997, ApJ, 487, 625

Greason, M. R., Offenberg, J. D., Cornett, R. H., Hill, R. S., & Stecher, T. P. 1994, PASP, 106, 1151

Hill, J. K., et al. 1997, ApJ, 477, 673

Hill, J. K., Bohlin, R. C., & Stecher, T. P. 1984, ApJ, 277, 542

Hill, R. S., et al. 1998, ApJ, 507, 179

Huizinga, J. E. 1994, PhDT, Univ. Groningen

Keel, W. C. 1996, AJ, 111 696

Kennicutt, R. C. 1998, ARA&A, 36, 189

Kent, S. M. 1983, ApJ, 266, 562

Kinney, A. L., Bohlin, R. C., Calzetti, D., Panagia, N., & Wyse, R. F. G. 1993, ApJS, 86, 5

Kuchinski, L. E., Madore, B. F., Freedman, W. L., & Trewhella, M. 2000, in preparation

Kuchinski, L. E., Terndrup, D. M., Gordon, K. D., & Witt, A. N. 1998, AJ, 115, 1438

Maoz, D., Filippenko, A. V., Ho, L. C., Macchetto, F. D., Rix, H.–W., & Schneider, D. P. 1996, ApJS, 107, 215

Marcum, P. M., et al. 1997, in The Ultraviolet Universe at Low and High Redshift, ed. W. H. Waller et al. (Woodbury, NY: AIP), 88

Marcum, P. M., et al. 2000, in preparation

Martin, C., et al. 1997, BAAS, 191, 63.04

Martin, P., & Roy, J.–R. 1994, ApJ, 424, 599

Meurer, G. R., Heckman, T. M., Leitherer, C., Kinney, A., Robert, C., & Garnett, D. R. 1995, AJ, 110, 2665

Mihalas, D. & Binney, J. 1981, Galactic Astronomy (San Francisco: W. H. Freeman)

O'Connell, R. W. 1999, to appear in ARA&A, 1999

O'Connell, R. W. 1997a, in The Ultraviolet Universe at Low and High Redshift, ed. W. H. Waller et al. (Woodbury, NY: AIP), 11

O'Connell, R. W. 1997b, in Star Formation Near and Far, ed. S. S. Holt & L. G. Mundy (New York: AIP), 491

O'Connell, R. W., & Marcum, P. M. 1996, in HST and the High Redshift Universe, ed. N. R. Tanvir, A. Aragon–Salamanca, & J. V. Wall (Singapore: World Scientific)

Ohl, R. G., et al. 1998, ApJ, 505, L11

Prugniel, P., & Heraudeau, P. 1998, A&AS, 128,299

Reichen, M., Kaufman, M., Blecha, A., Golay, M., & Huguenin, D. 1994, A&AS, 106, 523

Roberts, M. S., & Haynes, M. P. 1994, ARA&A, 32, 115

Sandage, A. 1961, The Hubble Atlas of Galaxies (Washington: Carnegie Institution of Washington)

Sandage, A., & Brucato, R. 1979, AJ, 84, 472

Smith, A. M., et al. 2000, ApJ, submitted

Smith, A. M., Collins, N. R., Waller, W. H., Fanelli, M. N., Stecher, T. P., & the UIT Team 1997, in The Ultraviolet Universe at Low and High Redshift, ed. W. H. Waller et al. (Woodbury, NY: AIP), 439

Smith, D. A., et al. 1996, ApJ, 473, L21

Stecher, T. P., Bohlin, R. C., Hill, J. K., & Jura, M. A. 1982, ApJ, 255, L99

Stecher, T. P., et al. 1997, PASP, 109, 58, 4

Storchi–Bergmann, T., Wilson, A. S., & Baldwin, J. A. 1996, ApJ, 472, 83

Stover, R. J. 1988, in Instrumentation for Ground–Based Optical Astronomy, ed. L. B. Robinson (New York: Springer), 443

Teplitz, H. I., Gardner, J. P., Malumuth, E. M., & Heap, S. R. 1998, ApJ, 507, L17

Tody, D. 1986, SPIE, 627, 733

Tully, R. B. 1988, Catalog of Nearby Galaxies, (Cambridge: Cambridge UP)

Waller, W. H., et al. 2000, AJ, submitted

Waller, W. H., et al. 1997a, ApJ, 481, 169

Waller, W. H., Fanelli, M. N., Collins, N. R., Cornett, R. H., Offenberg, J., Marcum, P. M., Stecher, T. P., & the UIT Science Team 1997b, in The Ultraviolet Universe at Low and High Redshift, ed. W. H. Waller et al. (Woodbury, NY: AIP), 39

Waller, W. H., Stecher, T. P., & the UIT Science Team 1997c, in Star Formation Near and Far, ed. S. S. Holt & L. G. Mundy (New York: AIP), 287

Waller, W. H., et al. 1995, AJ, 110, 1255

Williams, R. E., et al. 1996, AJ, 112. 1335

Witt, A. N., Petersohn, J. K., Bohlin, R. C., O'Connell, R. W., Roberts, M. S., Smith, A. M., & Stecher, T. P. 1992, ApJ, 395, L5

Yi, S., Lee, Y.–W., Woo, J.–H., Park, J.–H., Demarque, P., & Oemler, A. 1999, ApJ, 513, 128

Fig. 1.— FUV and optical images of sample galaxies. All images are registered to the FUV coordinate system and oriented with North up and East to the left. As noted in the text, the images are displayed such that pixels of the same brightness (flux) have constant gray level for all images of the same galaxy. Scale bars, which are relevant to all images of a particular galaxy, are shown on each of the FUV panels.

Fig. 2.— FUV and optical images of FUV–bright galaxies rescaled to show bright central regions. As in Figure 1, pixels of the same brightness have constant gray level on all images of a galaxy.

Fig. 3.— FUV and optical images of galaxies with red FUV–$V$ colors, renormalized so that optical data are not badly saturated in the display. Here, the optical data are displayed with a larger stretch than the FUV images in order to compare the central structure in both images.

Fig. 4.— FUV and optical surface brightness profiles of sample galaxies. The surface brightnesses are calibrated as described in the text, then offset by a constant to better show the relative shapes. Data from the optical filters are offset for ease of viewing; offsets are noted on each panel. Symbols for the different filters are as follows: FUV=filled diamonds, $U$=open circles, $B$=plus symbols, $V$=open triangles, $R$=open asterisks, $I$=open squares.

Fig. 5.— FUV–optical color profiles for early–type spiral galaxies. The galaxy name and constant offset (where applicable) are noted next to each profile.

Fig. 6.— FUV and optical images of circumnuclear and inner star–forming rings in early–type spirals. The images are aligned, oriented, and scaled as described in Figure 1.

Fig. 7.— Color profiles for early–type spirals with star–forming rings or circumnuclear star–formation. As in Figure 5, the galaxy name and constant offset are noted next to each profile. Locations of the rings and circumnuclear star–formation (CSF) regions are labeled for each galaxy.

Fig. 8.— Color profiles for late–type galaxies with flat FUV–optical color gradients. As in Figure 5, the galaxy name and constant offset are noted next to each profile.

Fig. 9.— Color profiles for late–type galaxies with central starbursts. As in Figure 5, the galaxy name and constant offset are noted next to each profile.

This 2-column preprint was prepared with the AAS LaTeX macros v4.0.

TABLE 1. Basic Data for UIT Sample Galaxies

| Name | $\alpha$ (2000)[a] | $\delta$ (2000)[a] | Type[b] | Activity[b] | D[c] | $A_B$[c] | $\epsilon$[e] | P. A.[f] |
|---|---|---|---|---|---|---|---|---|
| NGC 925 | 02 27 16.8 | +33 34 41 | SAB(s)d | ... | 9.4 | 0.25 | 0.40 | 115 |
| NGC 1068 (M 77) | 02 42 40.2 | −00 00 48 | RSA(rs)b | Sy 2 | 14.4 | 0.05 | 0.20 | 84 |
| NGC 1097 | 02 46 18.9 | −30 16 21 | SB(s)b | Sy 1 | 14.5 | 0.07 | 0.32 | 140 |
| NGC 1313 | 03 18 15.5 | −66 29 51 | SB(s)d | ... | 3.7 | 0.03 | 0.20 | 40 |
| NGC 1365 | 03 33 36.6 | −36 08 17 | SB(s)b | Sy 1.8 | 16.9 | 0.00 | 0.45 | 32 |
| NGC 1510 | 04 03 32.6 | −43 24 01 | S0,pec | H II | 10.3 | 0.00 | 0.12 | 115 |
| NGC 1512 | 04 03 54.6 | −43 21 03 | SB(r)a | ... | 9.5 | 0.00 | 0.36 | 56 |
| NGC 1566 | 04 20 00.4 | −54 56 18 | SAB(s)bc | Sy 1 | 13.4 | 0.00 | 0.21 | 40 |
| NGC 1672 | 04 45 42.2 | −59 14 57 | SB(s)b | Sy 2 | 14.5 | 0.00 | 0.13 | 161 |
| NGC 2403 | 07 36 54.5 | +65 35 58 | SAB(s)cd | ... | 4.2 | 0.16 | 0.44 | 115 |
| NGC 2841 | 09 22 01.8 | +50 58 31 | SA(r)b | LINER, Sy 1 | 12.0 | 0.00 | 0.56 | 147 |
| NGC 2903 | 09 32 09.7 | +21 30 02 | SAB(rs)bc | H II | 6.3 | 0.07 | 0.53 | 24 |
| NGC 3115 | 10 05 14.1 | −07 43 07 | S0 | ... | 6.7 | 0.10 | 0.66[g] | 43[f] |
| NGC 3226 | 10 23 27.4 | +19 53 55 | E2*,pec | LINER | 23.4 | 0.02 | 0.20 | 10 |
| NGC 3227 | 10 23 31.5 | +19 51 48 | SAB(s)a,pec | Sy 1.5 | 20.6 | 0.02 | 0.55 | 157 |
| IC 2574 | 10 28 22.5 | +68 24 39 | SAB(s)m | ... | 2.7 | 0.06 | 0.59 | 62 |
| NGC 3310 | 10 38 46.1 | +53 30 08 | SAB(r)bc,pec | H II | 18.7 | 0.00 | 0.22 | 170 |
| NGC 3351 (M 95) | 10 43 58.0 | +11 42 15 | SB(r)b | H II | 8.1 | 0.04 | 0.32 | 17 |
| NGC 3379 (M 105) | 10 47 49.9 | +12 34 57 | E1 | ... | 8.1 | 0.05 | 0.13 | 65 |
| NGC 3384 | 10 48 17.2 | +12 37 49 | SB0* | ... | 8.1 | 0.05 | 0.50 | 51 |
| NGC 3389 | 10 48 27.9 | +12 32 01 | SA(s)c | ... | 22.5 | 0.06 | 0.55 | 108 |
| NGC 4038 | 12 01 52.9 | −18 51 54 | SB(s)m,pec | ... | 25.5 | 0.05 | 0.00[h] | ... |
| NGC 4039 | 12 01 53.9 | −18 53 06 | SA(s)m,pec | ... | 25.3 | 0.05 | 0.00[h] | ... |
| NGC 4151 | 12 10 33.0 | +39 24 28 | SAB(rs)ab*,Pec | Sy 1.5 | 20.3 | 0.00 | 0.36 | 145 |
| NGC 4156 | 12 10 49.7 | +39 28 24 | SB(rs)b | LINER | 90.4[i] | 0.00 | 0.20 | 45 |
| NGC 4214 | 12 15 39.5 | +36 19 39 | IAB(s)m | H II | 3.5 | 0.00 | 0.18 | 132 |
| NGC 4449 | 12 28 11.4 | +44 05 40 | IBm | ... | 3.0 | 0.00 | 0.46 | 60 |
| NGC 4647 | 12 43 32.4 | +11 34 56 | SAB(rs)c | ... | 16.8 | 0.04 | 0.20 | 135 |
| NGC 4649 (M 60) | 12 43 40.3 | +11 32 58 | E2 | ... | 16.8 | 0.04 | 0.17 | 130 |
| NGC 4736 (M 94) | 12 50 53.6 | +41 07 10 | (R)SA(r)ab | LINER | 4.3 | 0.00 | 0.22 | 95 |
| NGC 5055 (M 63) | 13 15 49.3 | +42 02 06 | SA(rs)bc | H II, LINER | 7.2 | 0.00 | 0.47 | 102 |
| NGC 5194 (M 51) | 13 29 53.3 | +47 11 48 | SA(s)bc,pec | Sy 2.5 | 7.7 | 0.00 | 0.30 | 30 |
| NGC 5236 (M 83) | 13 37 00.3 | −29 52 04 | SAB(s)c | H II | 4.7 | 0.14 | 0.10 | 80 |
| NGC 5253 | 13 39 55.9 | −31 38 41 | Pec | H II | 3.2 | 0.19 | 0.57 | 43 |
| NGC 5457 (M 101) | 14 03 12.5 | +54 20 55 | SAB(rs)cd | ... | 5.4 | 0.00 | 0.00 | ... |

[a] Data from the *RC*3.

[b] Nuclear activity classification, from the NASA Extragalactic Database (NED).

[c] Distances in Mpc from Tully 1988 ($H_0 = 75$ km/s/Mpc), except as noted.

[d] Foreground Galactic extinction values from Burstein & Heiles 1984.

[e] Adopted ellipticity for azimuthal averaging in surface brightness profile calculations, defined as $\epsilon = 1 - \frac{b}{a}$.

[f] Adopted major axis position angle for azimuthal averaging in surface brightness profile calculations.

[g] An ellipticity of 0.29 and a P. A. of 118 were used for the FUV image of NGC 3115, which was never registered to the optical data (see Section 3).

[h] NGC 4038/9 is treated as one galaxy for profile calculation, see Section 3.

[i] Distance from $V_{GSR}$, $H_0 = 75$ km/s/Mpc.

Table 2. Observations of Sample Galaxies

| Name | UV Date | UV(Filter)[a] | Optical Date | Telescope[b] | $U$[a] | $B$[a] | $V$[a] | $R$[a] | $I$[a] |
|---|---|---|---|---|---|---|---|---|---|
| NGC 925 | 950314 | 1591 (B5) | 990207 | Pal1.5 | ⋯ | ⋯ | ⋯ | 300[c] | ⋯ |
| | | | 990213 | Pal1.5 | 3600[c] | 600 | 600 | ⋯ | ⋯ |
| NGC 1068 | 950307 | 753 (B5) | 990214 | Pal1.5 | 3600 | 300 | 300 | 200 | ⋯ |
| NGC 1097[d] | 950312 | 1121 (B5) | 951221 | LCO2.5 | 3x400 | 3x200 | 3x200 | ⋯ | 3x200 |
| NGC 1313[d] | 950312 | 1071 (B5) | 951224 | LCO2.5 | 2x400 | 2x200 | 2x200 | ⋯ | 2x200 |
| NGC 1365[d] | 950315 | 974 (B5) | 951223 | LCO2.5 | 2x400 | 2x200 | 2x200 | ⋯ | 2x200 |
| NGC 1512[d]/10[e] | 950315 | 949 (B5) | 951220 | LCO2.5 | 3x400 | 3x200 | 3x200 | ⋯ | 3x200 |
| NGC 1566 | 950316 | 1391 (B5) | 951222 | LCO2.5 | 2x400 | 2x200 | 2x200 | ⋯ | 2x200 |
| NGC 1672 | 950307 | 927 (B5) | 951219 | LCO2.5 | 4x400 | 3x200 | 3x200 | ⋯ | 3x200 |
| NGC 2403[d] | 950308 | 772 (B1) | 971031 | Pal1.5 | 1600 | 600 | 300 | ⋯ | 300 |
| | | | 990208 | Pal1.5 | ⋯ | ⋯ | ⋯ | 60 | ⋯ |
| NGC 2841 | 950308 | 1021 (B1) | 940214 | Pal5.0 | ⋯ | 300 | ⋯ | ⋯ | 120,2x60 |
| | | | 990213 | Pal1.5 | 3600 | ⋯ | 300 | 200 | ⋯ |
| NGC 2903 | 950307 | 549 (B1) | 951123 | Pal1.5 | ⋯ | 900 | 600 | ⋯ | 600 |
| | | | 990208 | Pal1.5 | ⋯ | ⋯ | ⋯ | 300 | ⋯ |
| | | | 990214 | Pal1.5 | 3600 | ⋯ | ⋯ | ⋯ | ⋯ |
| NGC 3115 | 950307 | 1081 (B1) | 951226 | LCO2.5 | 300 | ⋯ | 300 | ⋯ | 300 |
| NGC 3226/7[e] | 950316 | 1271 (B1) | 960218 | Pal1.5 | ⋯ | 450 | ⋯ | ⋯ | ⋯ |
| | | | 990207 | Pal1.5 | ⋯ | ⋯ | ⋯ | 300 | ⋯ |
| IC 2574[d] | 950316 | 624 (B1) | 960414 | Pal5.0 | ⋯ | ⋯ | 3x600 | ⋯ | 5x400[c] |
| | | | 990208 | Pal1.5 | ⋯ | ⋯ | ⋯ | 300[c] | ⋯ |
| | | | 990214 | Pal1.5 | 3600 | 600 | ⋯ | ⋯ | ⋯ |
| NGC 3310 | 950311 | 1131 (B1) | 990207 | Pal1.5 | ⋯ | ⋯ | ⋯ | 300[c] | ⋯ |
| | | | 990214 | Pal1.5 | ⋯ | ⋯ | 300 | ⋯ | ⋯ |
| NGC 3351 | 950306 | 881 (B1) | 960118 | Pal1.5 | ⋯ | 600 | 300 | ⋯ | 2x600,300 |
| | | | 990208 | Pal1.5 | ⋯ | ⋯ | ⋯ | 300[c] | ⋯ |
| NGC 3379/84/89[e] | 950306 | 1301 (B1) | 990208 | Pal1.5 | ⋯ | ⋯ | ⋯ | 120 | ⋯ |
| NGC 4038/9[d] | 950307 | 881 (B1) | 951222 | LCO2.5 | 1200 | ⋯ | 600 | ⋯ | 600 |
| NGC 4151/6 [e] | 950313 | 833 (B1) | 990207 | Pal1.5 | ⋯ | ⋯ | ⋯ | 300 | ⋯ |
| NGC 4214 | 950313 | 1061 (B1) | 960514 | Pal1.5 | ⋯ | 600 | 2x300 | ⋯ | 300[c] |
| | | | 990208 | Pal1.5 | ⋯ | ⋯ | ⋯ | 300[c] | ⋯ |
| NGC 4449 | 950307 | 987 (B1) | 960515 | Pal1.5 | ⋯ | 600 | 300 | ⋯ | 300 |
| | | | 990207 | Pal1.5 | ⋯ | ⋯ | ⋯ | 300 | ⋯ |
| NGC 4647/9[e] | 950311 | 1301 (B1) | 990207 | Pal1.5 | ⋯ | ⋯ | ⋯ | 300 | ⋯ |
| NGC 4736 | 950312 | 1041 (B1) | 990208 | Pal1.5 | ⋯ | 2x600 | ⋯ | 300[c] | ⋯ |
| | | | 990213 | Pal1.5 | 3600 | ⋯ | ⋯ | ⋯ | ⋯ |
| | | | 990320 | Pal1.5 | ⋯ | ⋯ | 300 | ⋯ | ⋯ |
| NGC 5055[d] | 950315 | 1141 (B1) | 990213 | Pal1.5 | 3600 | 600 | 300 | 200 | ⋯ |
| NGC 5194[d] | 950312 | 1101 (B1) | 980423 | Pal1.5 | 6x1800 | ⋯ | ⋯ | ⋯ | ⋯ |
| | | | 990207 | Pal1.5 | ⋯ | 900 | 600 | 300 | 300 |
| NGC 5236[d] | 950306 | 819 (B1) | 960623 | CTIO1.5 | 4x300 | 4x300 | ⋯ | 4x300 | 4x60 |
| NGC 5253 | 950307 | 727 (B5) | 951222 | LCO2.5 | ⋯ | 300 | ⋯ | ⋯ | ⋯ |
| | | | 951223 | LCO2.5 | ⋯ | ⋯ | 3x600 | ⋯ | 2x600 |
| NGC 5457[d] | 950311 | 1311 (B1) | 960515 | Pal1.5 | ⋯ | 600 | 300 | ⋯ | 300 |

[a]Exposure time in seconds. (UV filter in parentheses).

[b]LCO2.5 = Las Campanas 2.5m, CTIO1.5 = Cerro Tololo 1.5m, Pal5.0 = Palomar 5m, Pal1.5 = Palomar 1.5m.

[c]Calibration estimated from other galaxies observed on the same night (see Section 2.4).

[d]Optical sky background uncertain because galaxy fills the frame.

[e]Galaxies imaged on same frame.

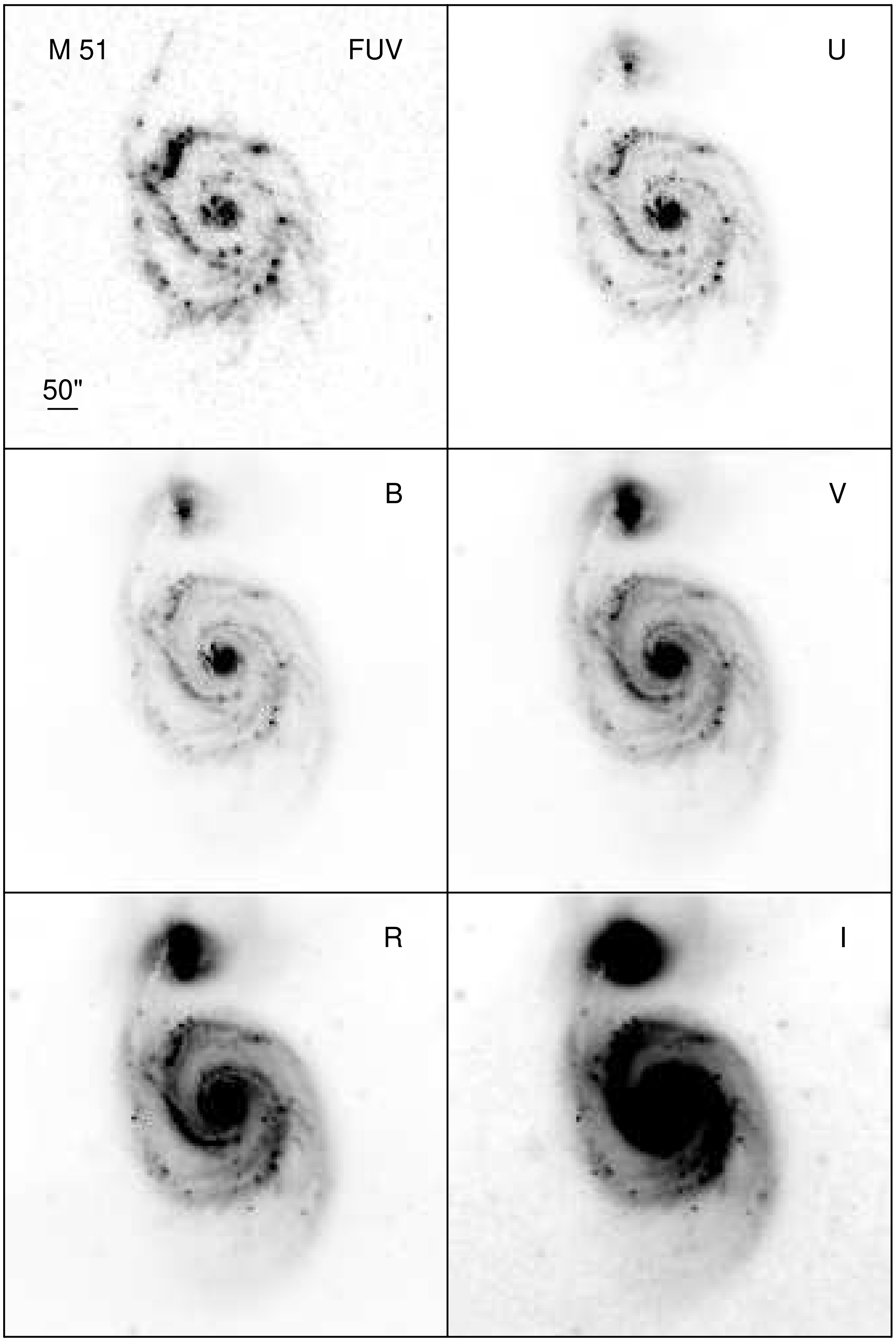


Fig. 1a.—

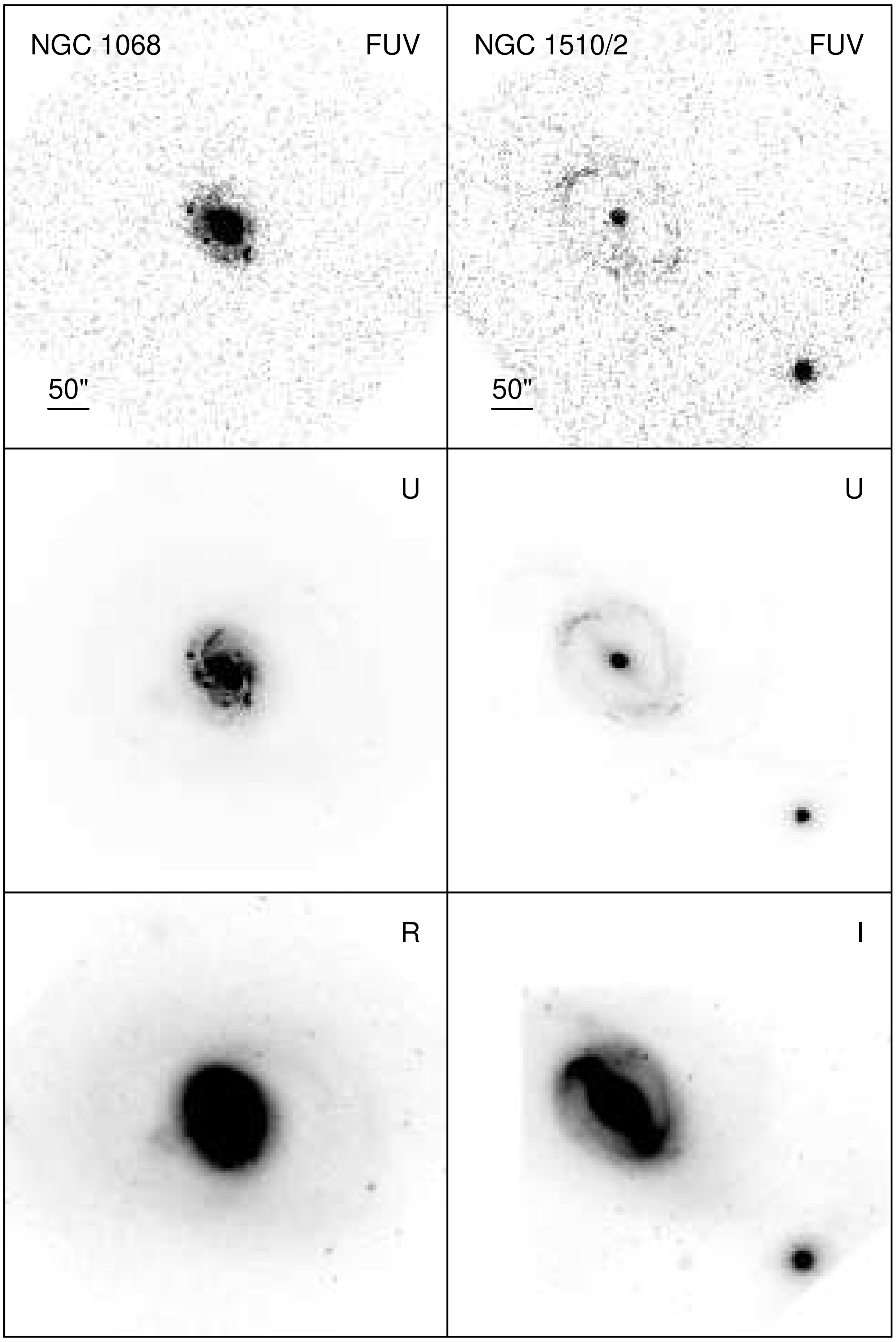


Fig. 1b.—

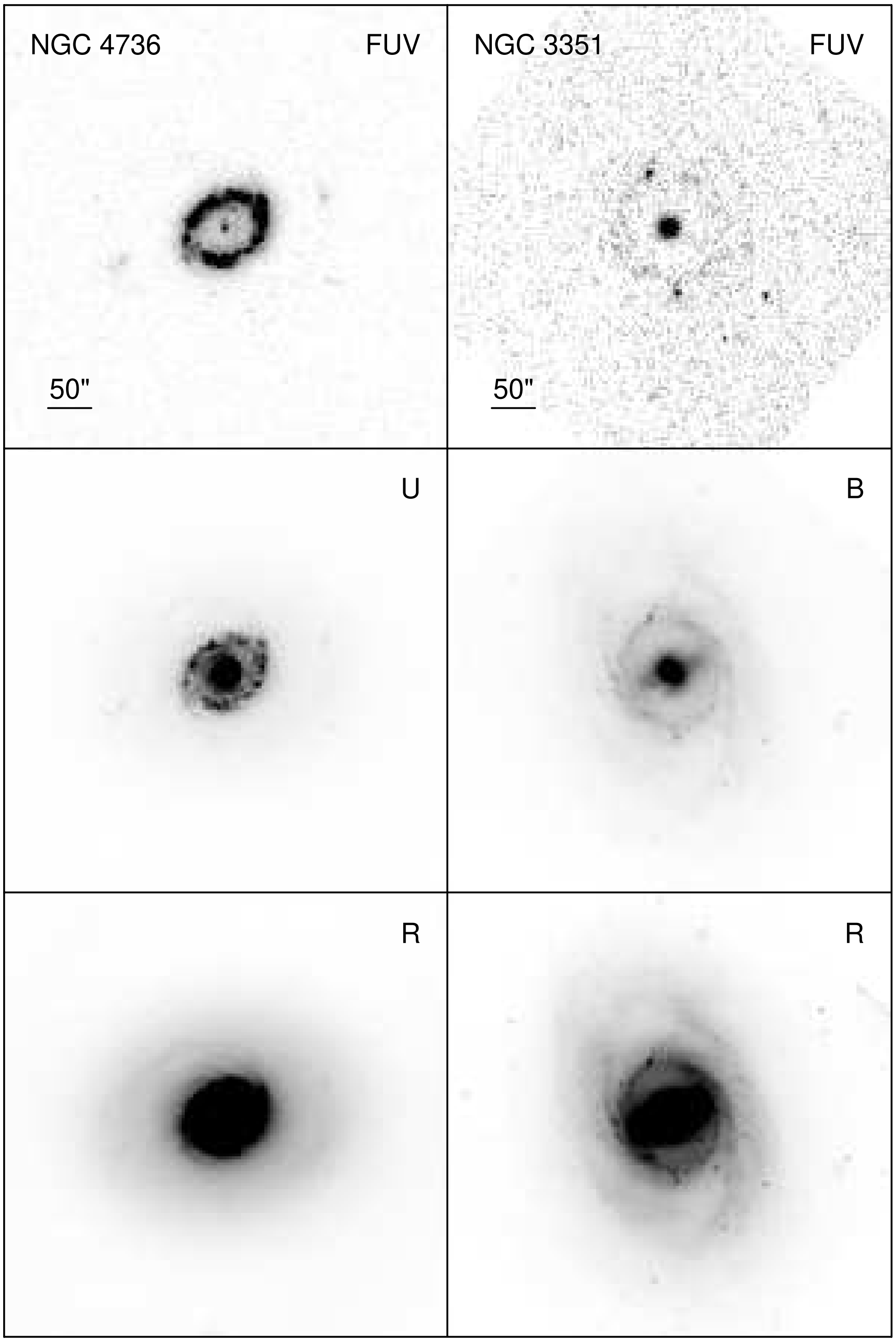


Fig. 1c.—

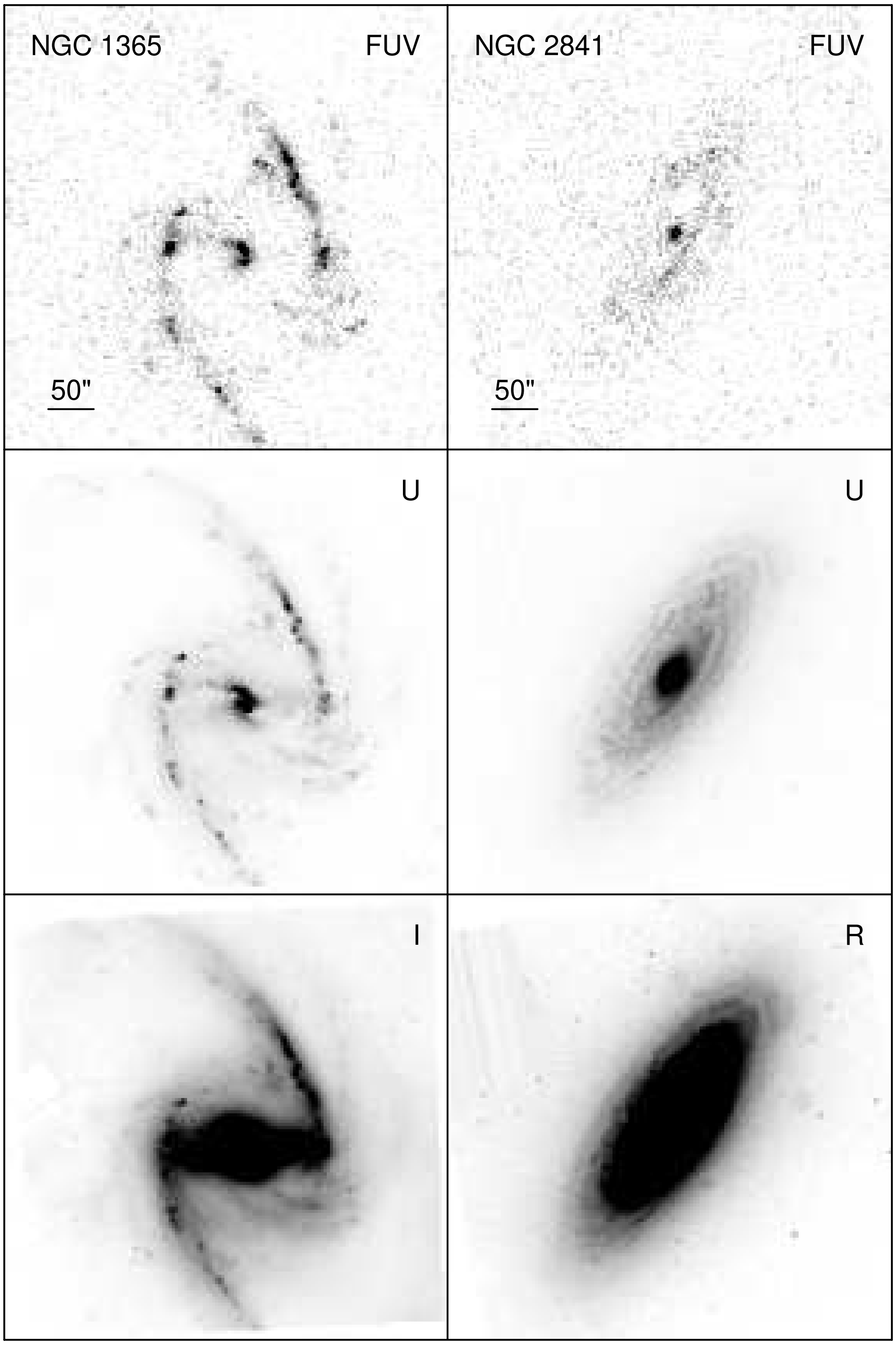


Fig. 1d.—

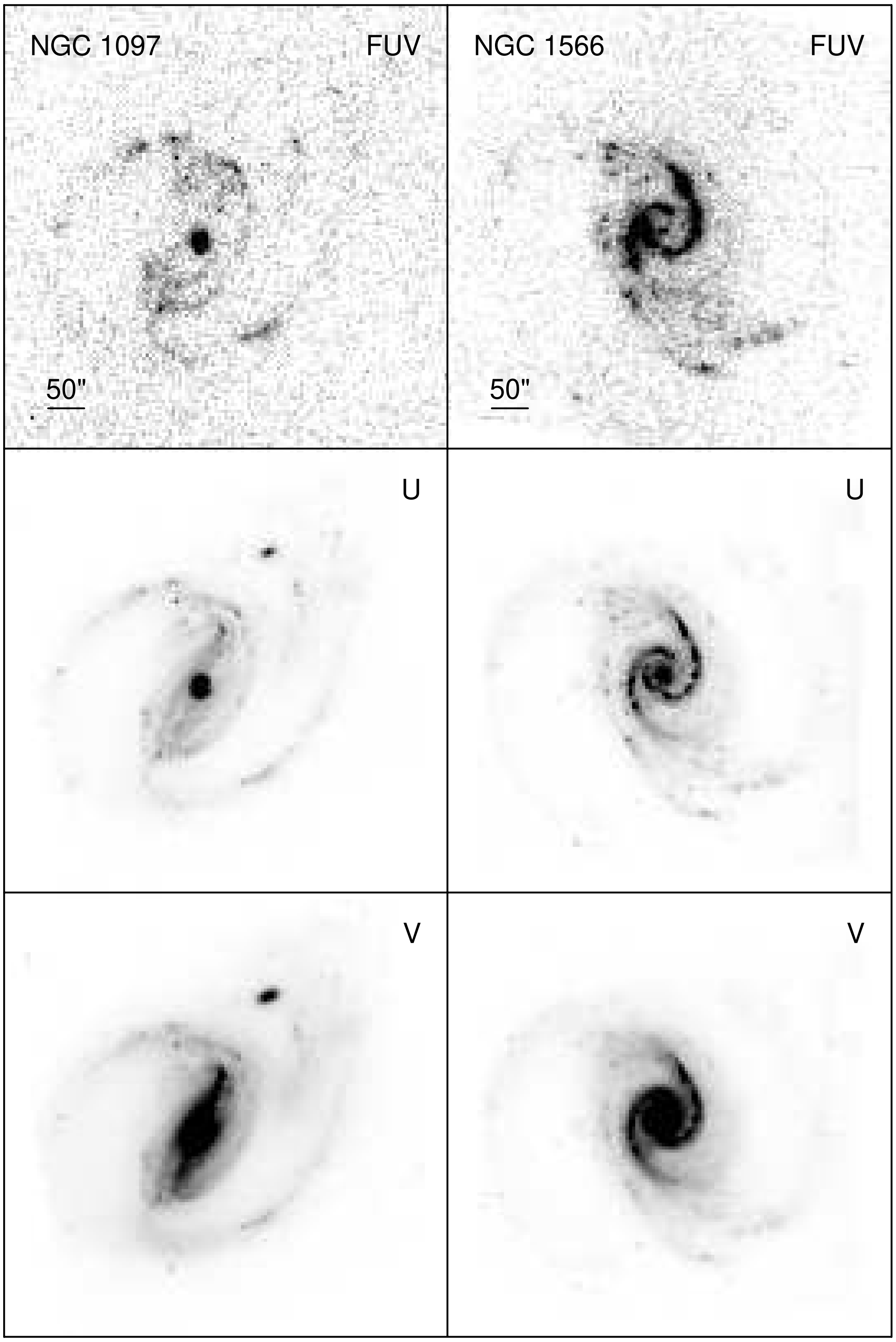


Fig. 1e.—

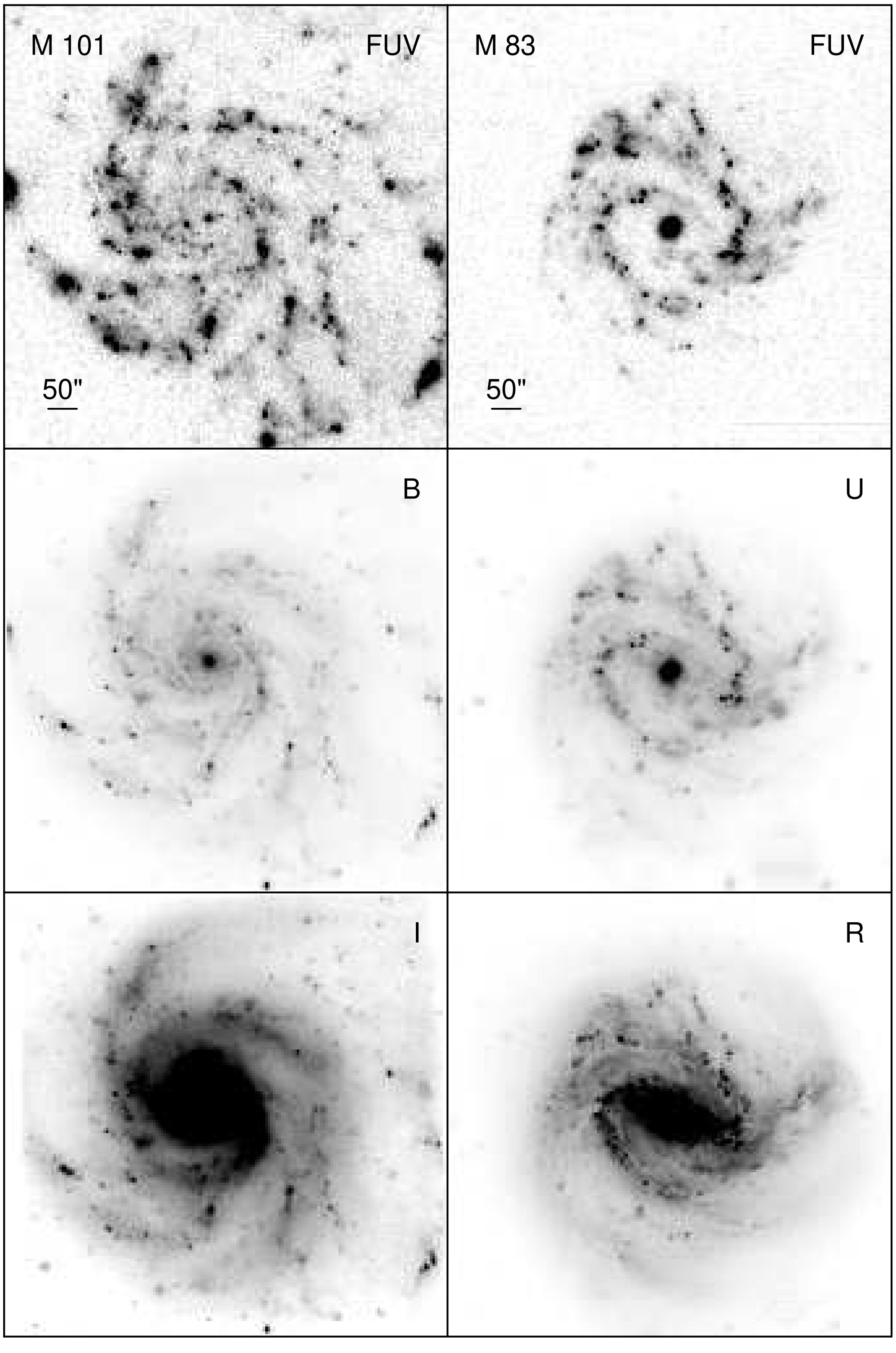


Fig. 1f.—

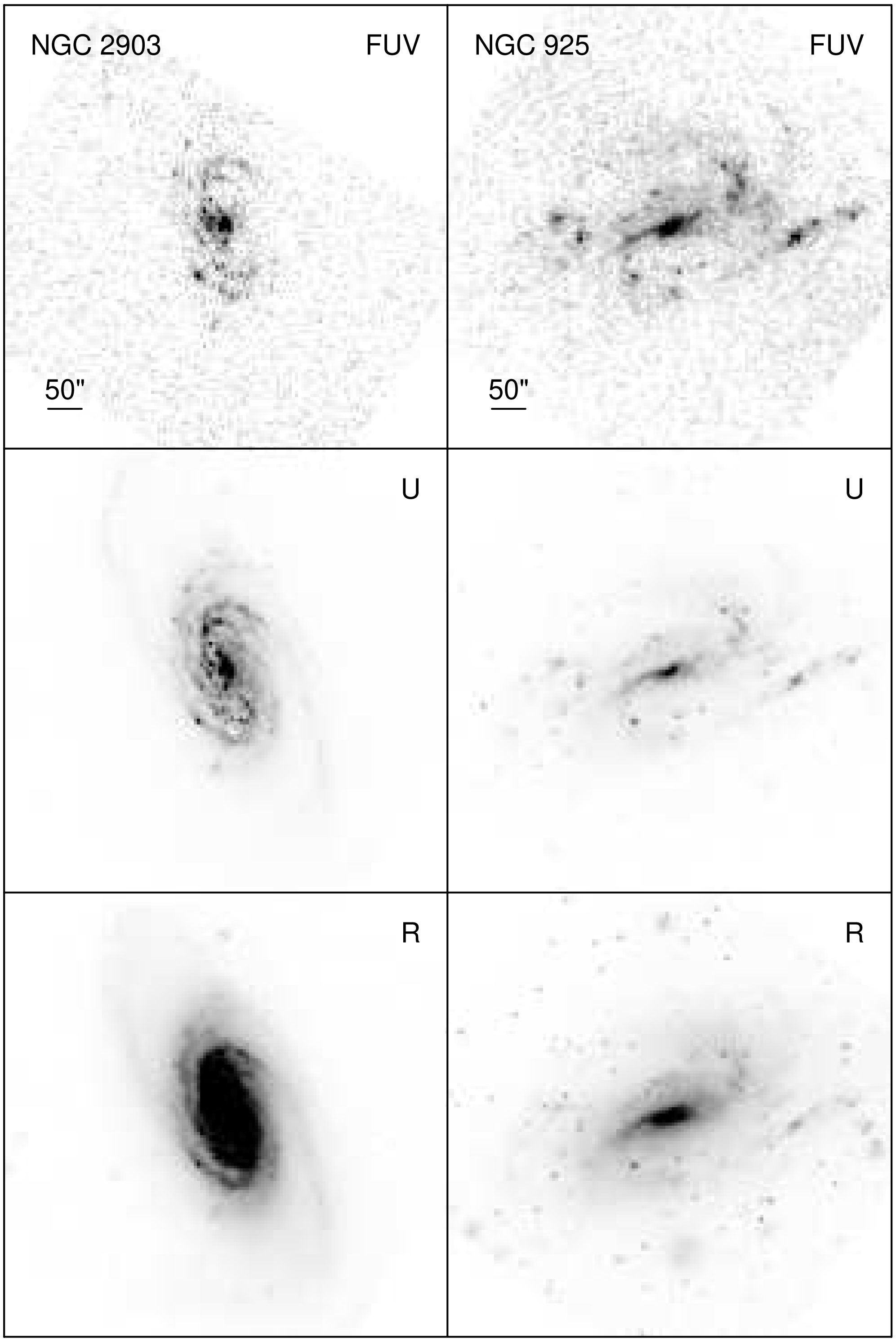


Fig. 1g.—

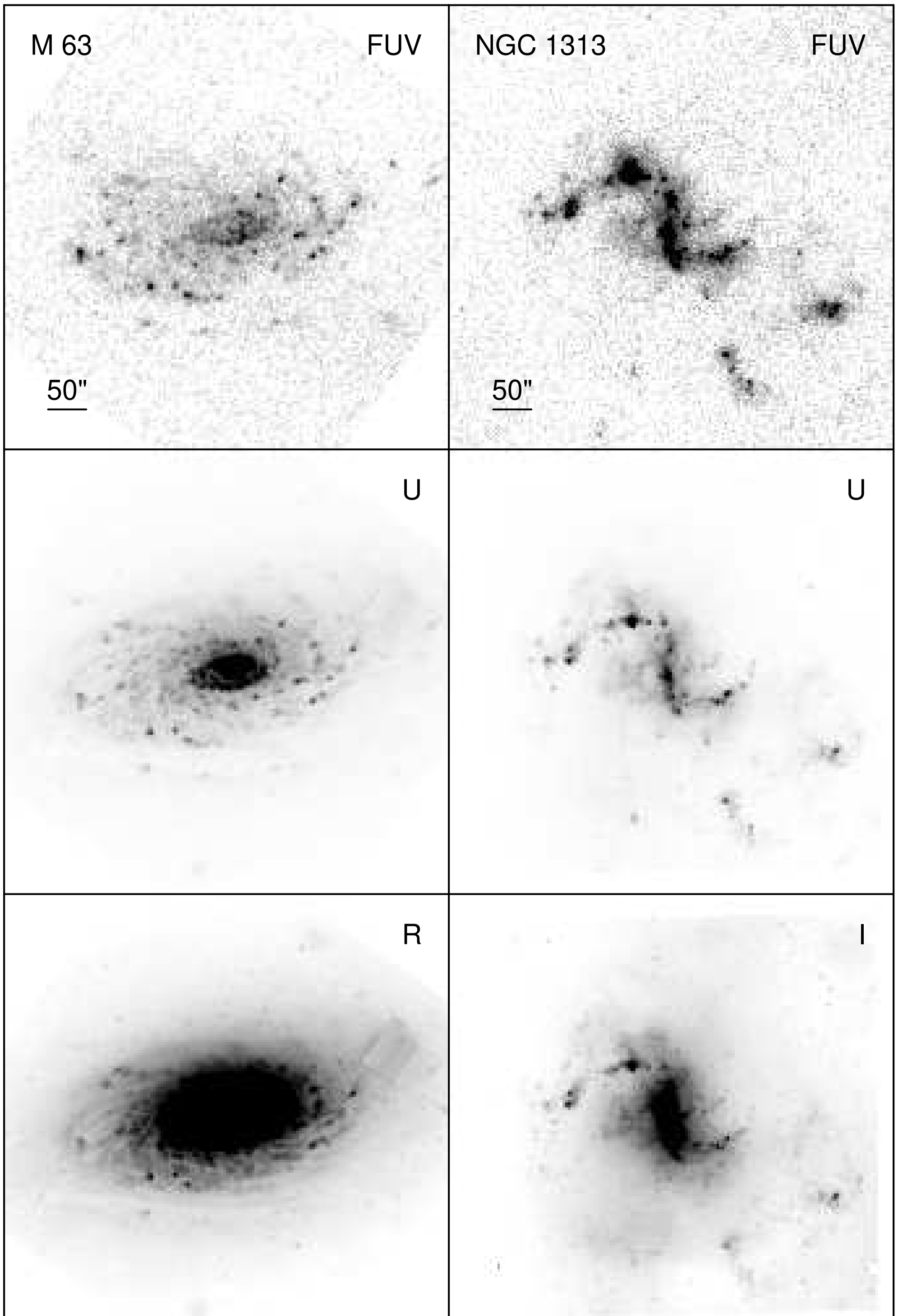


Fig. 1h.—

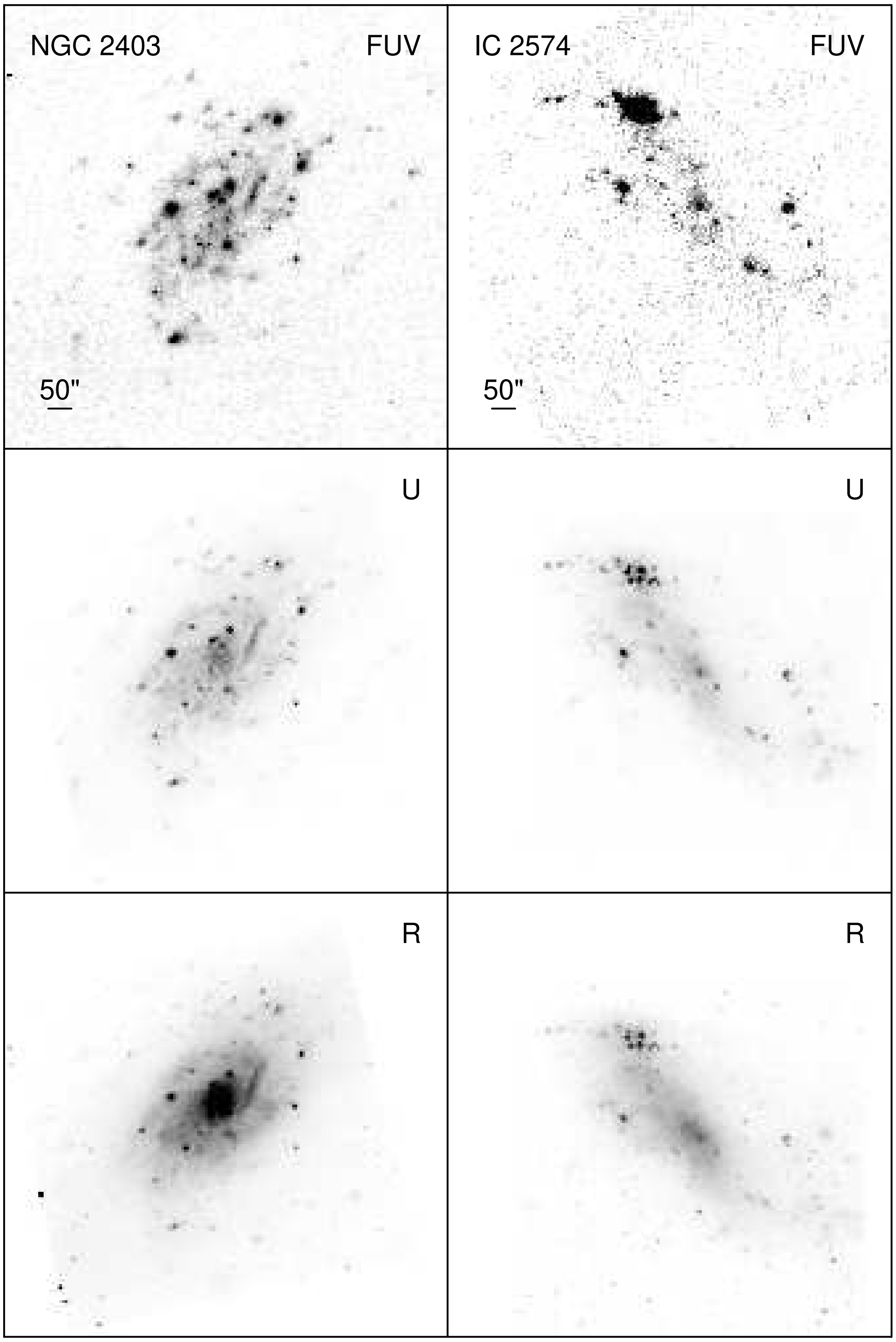


Fig. 1i.—

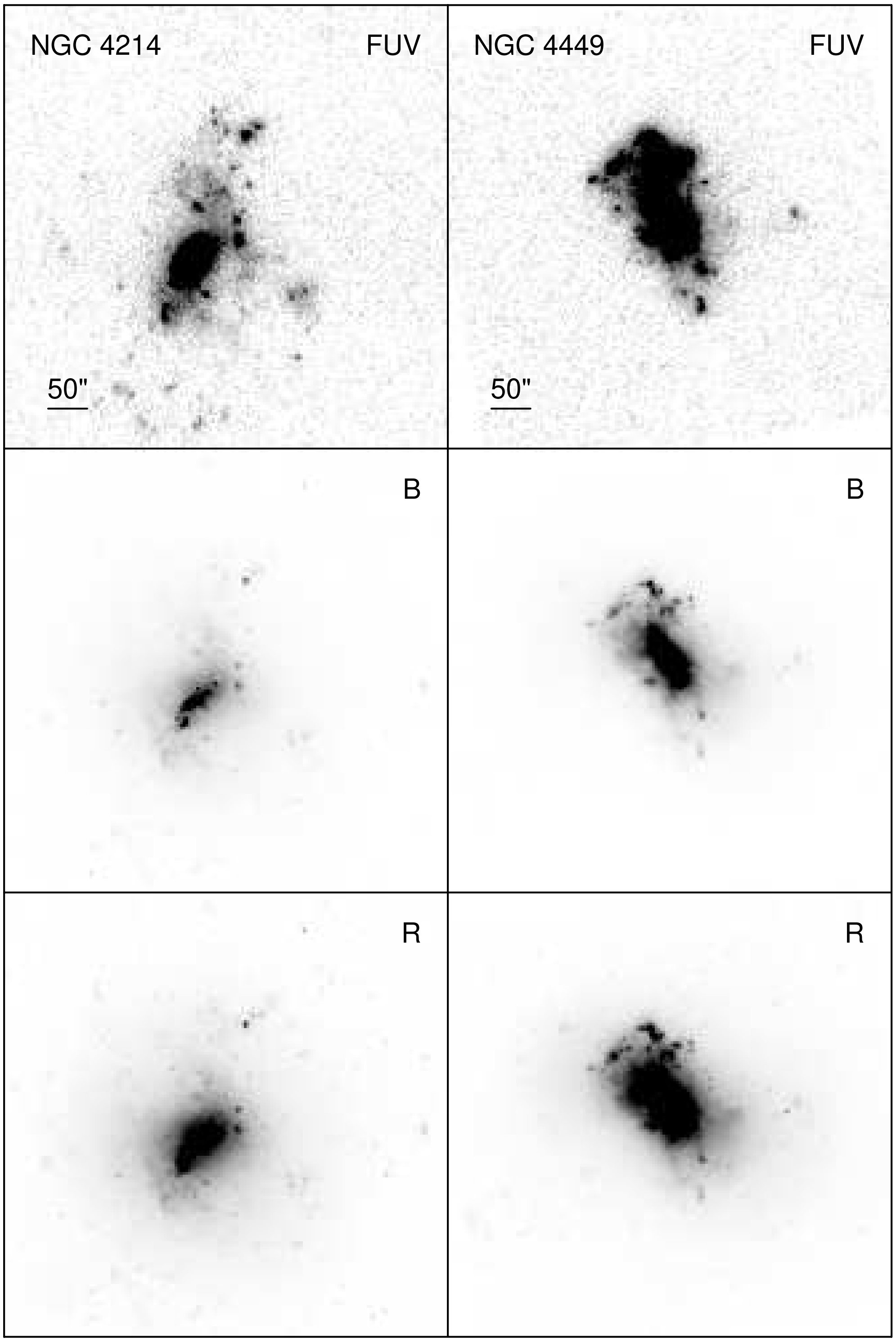


Fig. 1j.—

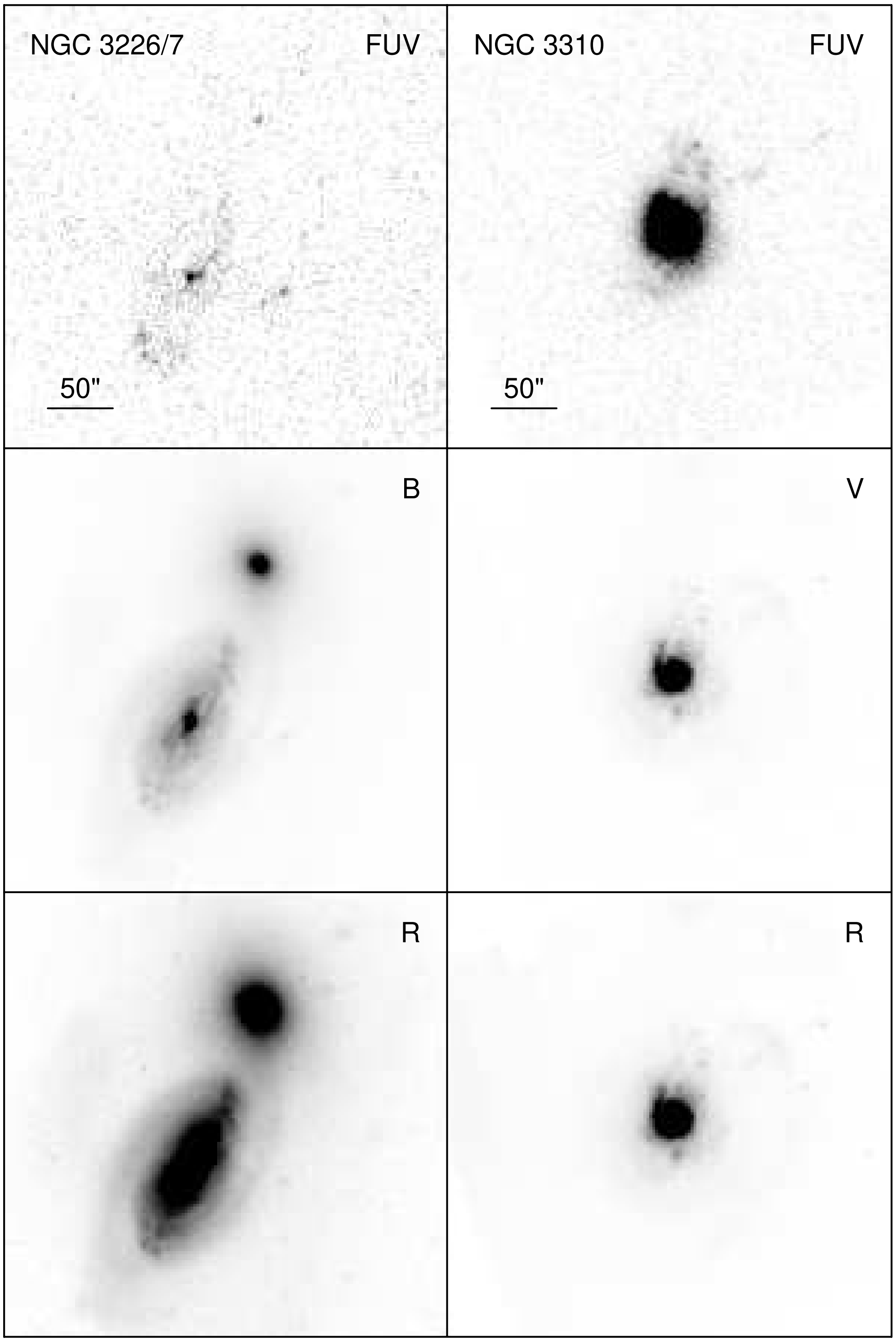


Fig. 1k.—

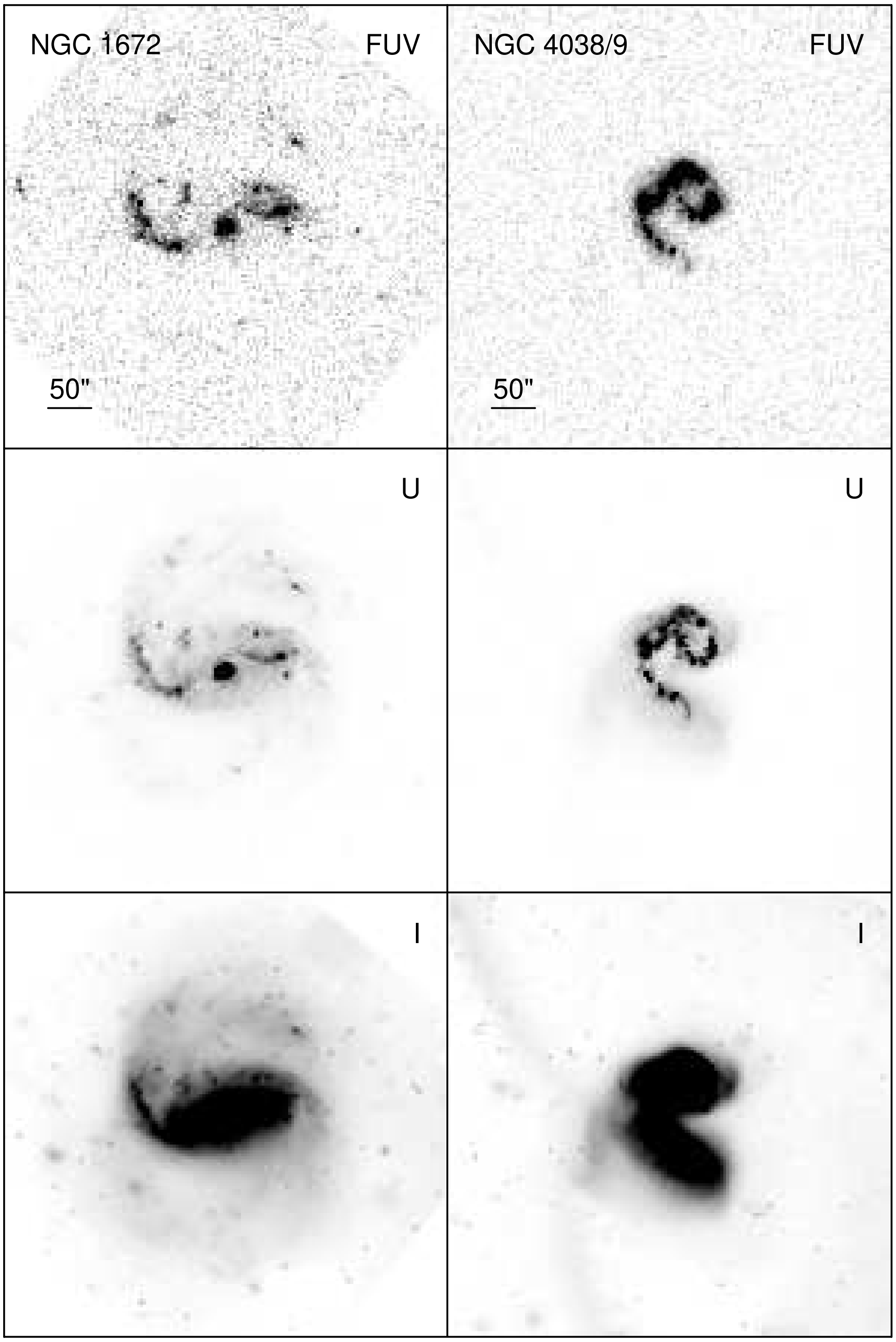


Fig. 11.—

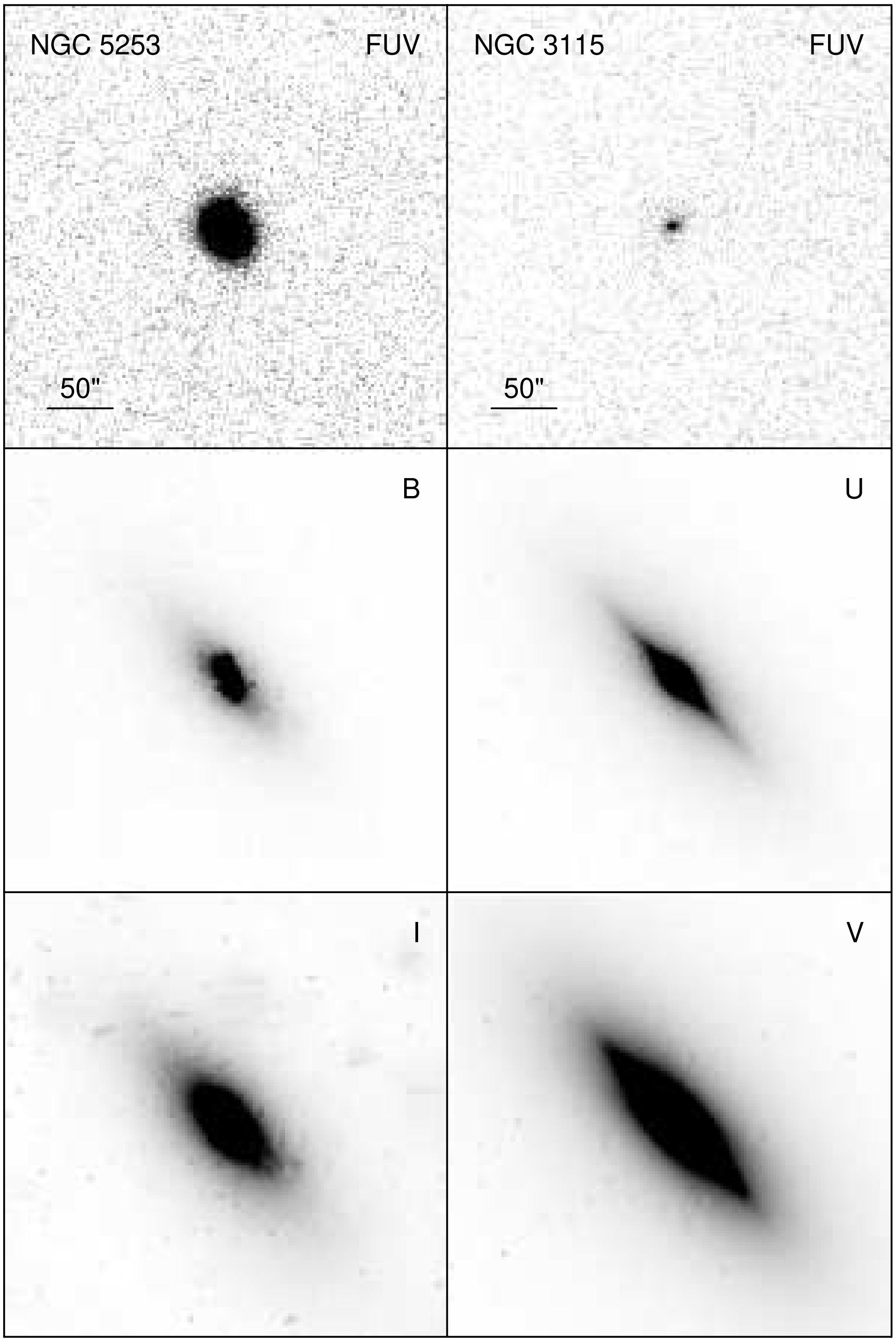


Fig. 1m.—

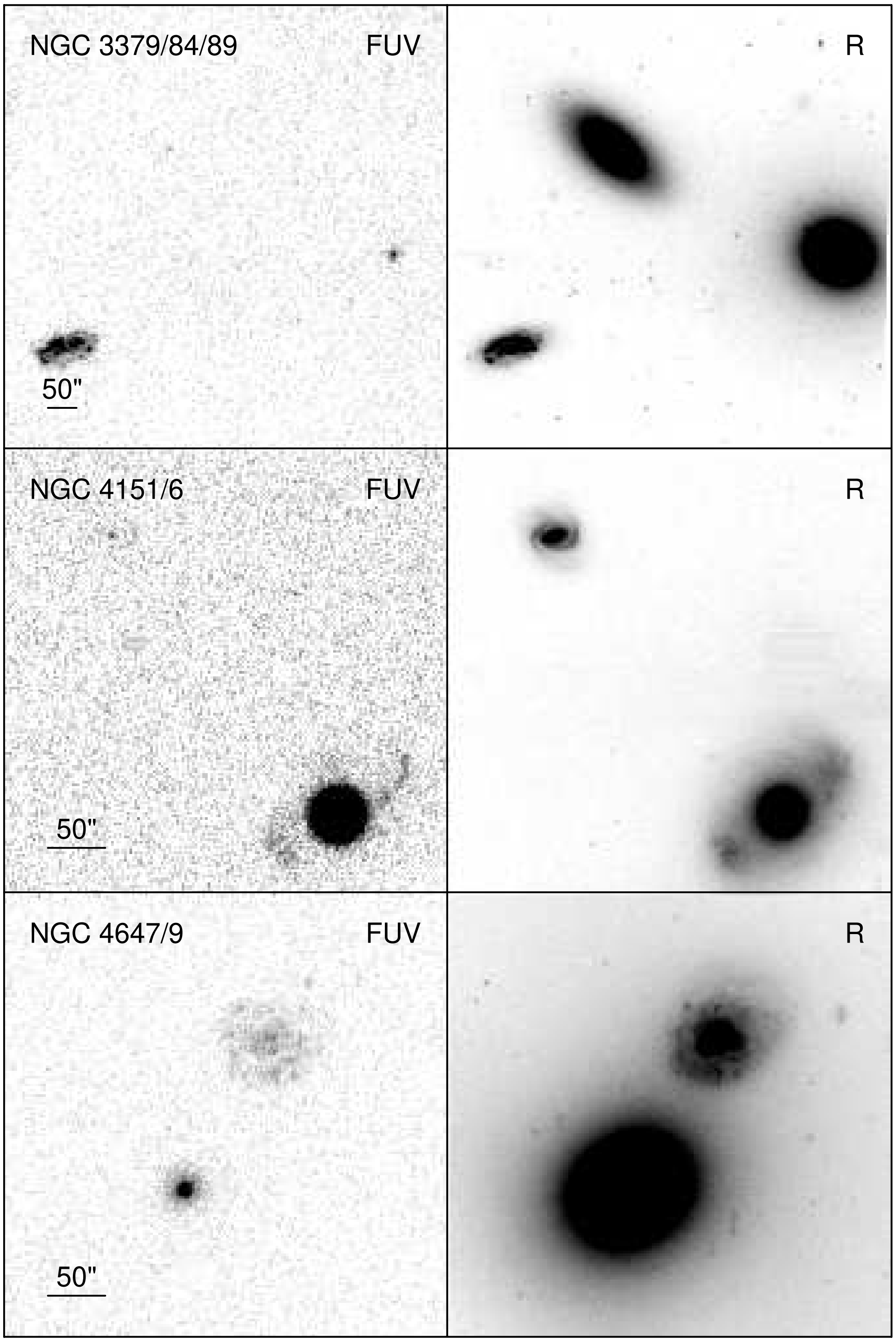


Fig. 1n.—

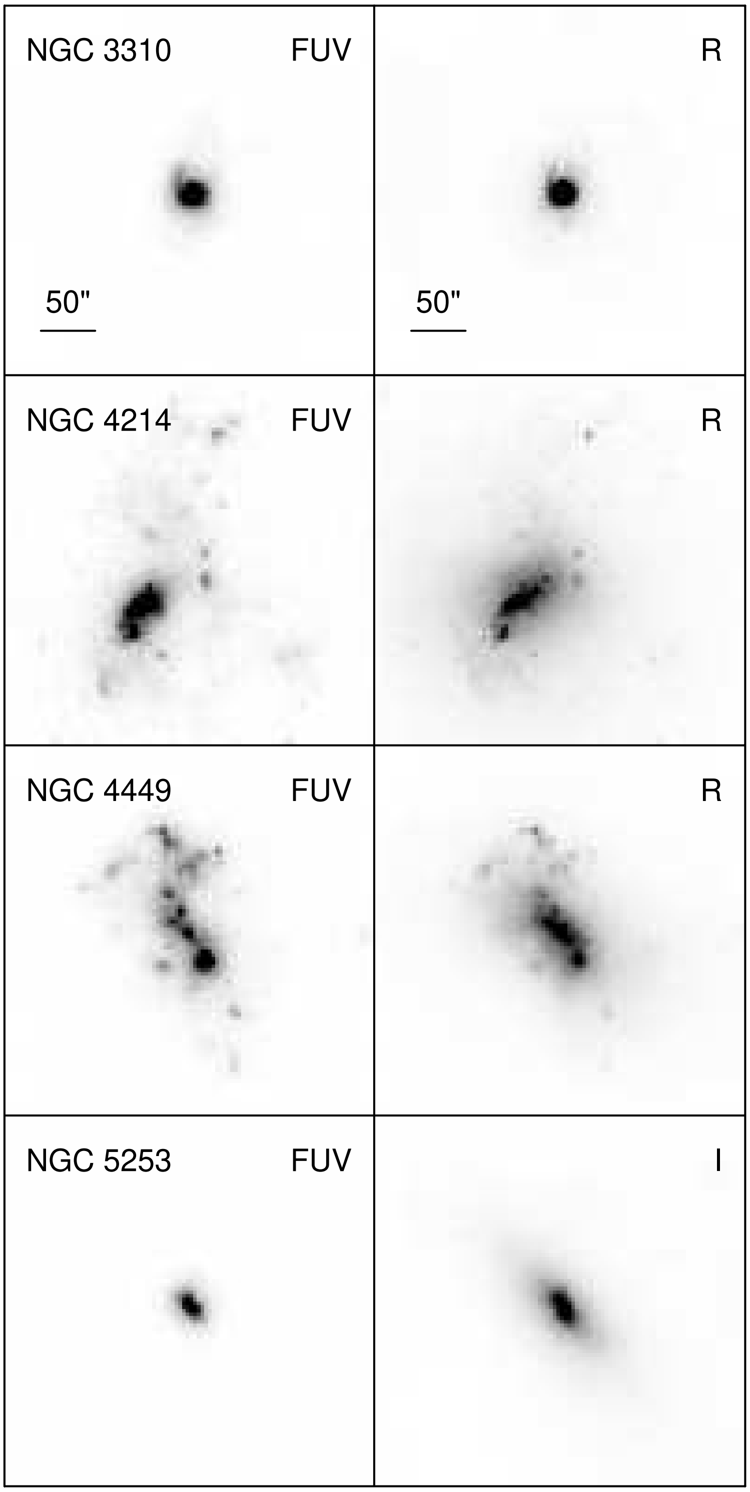


Fig. 2.—

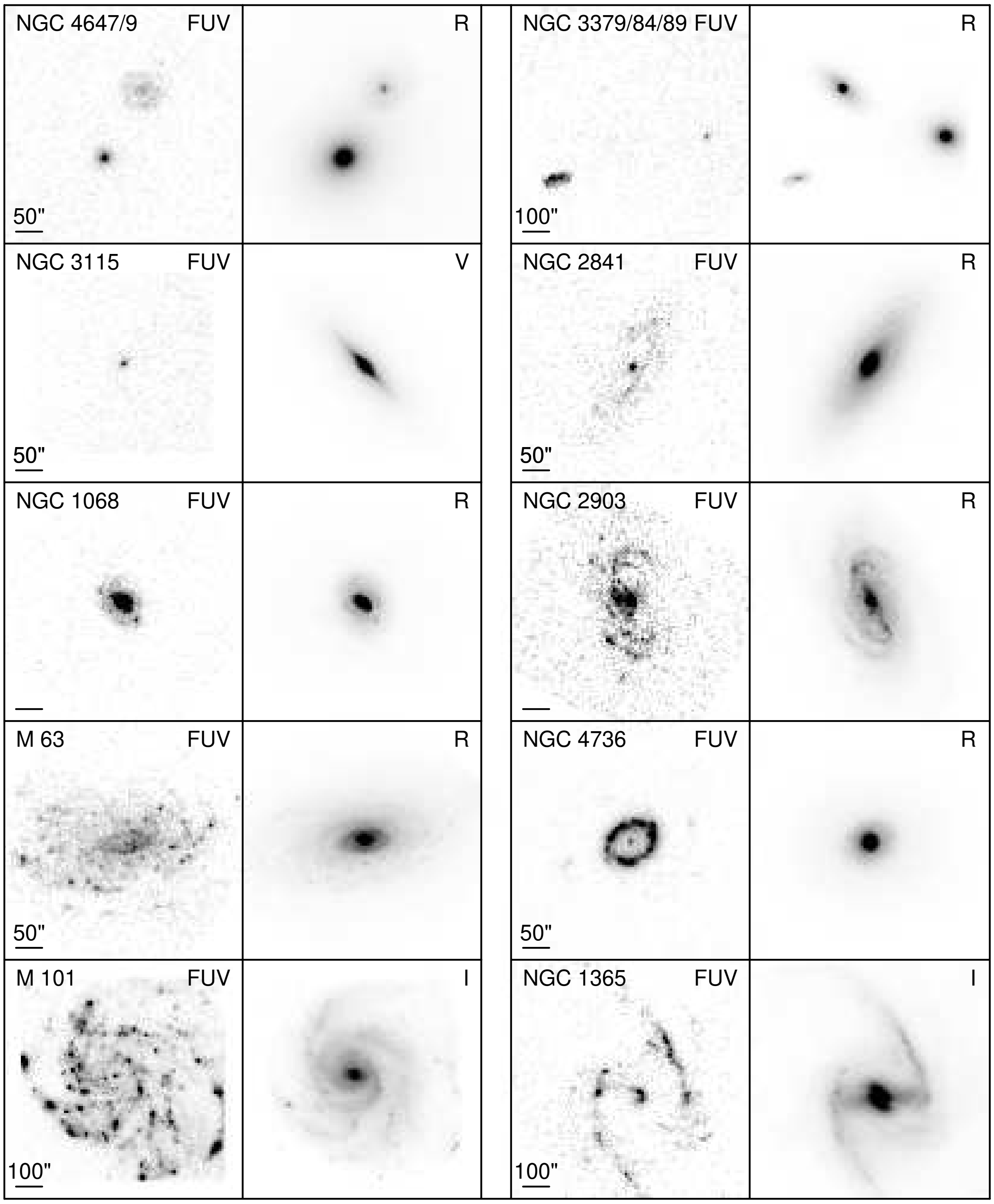
NGC 4647/9
FUV
R
50"
NGC 3379/84/89 FUV
R
100"
NGC 3115
FUV
V
50"
NGC 2841
FUV
R
50"
NGC 1068
FUV
R
NGC 2903
FUV
R
M 63
FUV
R
50"
NGC 4736
FUV
R
50"
M 101
FUV
I
100"
NGC 1365
FUV
I
100"

Fig. 3.—

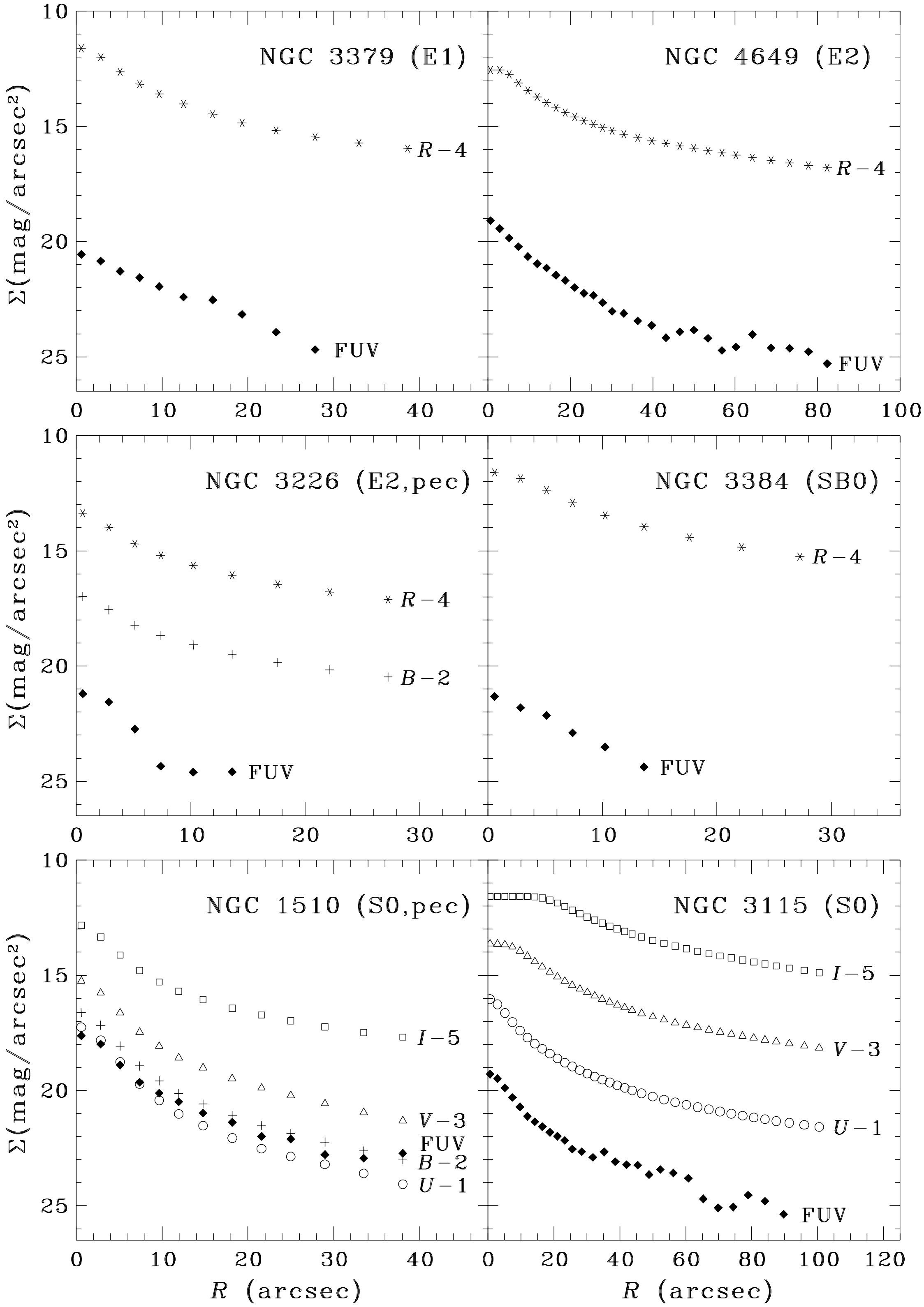

NGC 3379 (E1)
R−4
FUV
NGC 4649 (E2)
R−4
FUV
NGC 3226 (E2,pec)
R−4
B−2
FUV
NGC 3384 (SB0)
R−4
FUV
NGC 1510 (S0,pec)
I−5
V−3
FUV
B−2
U−1
NGC 3115 (S0)
I−5
V−3
U−1
FUV
Σ(mag/arcsec²)
R (arcsec)




Fig. 4a.—

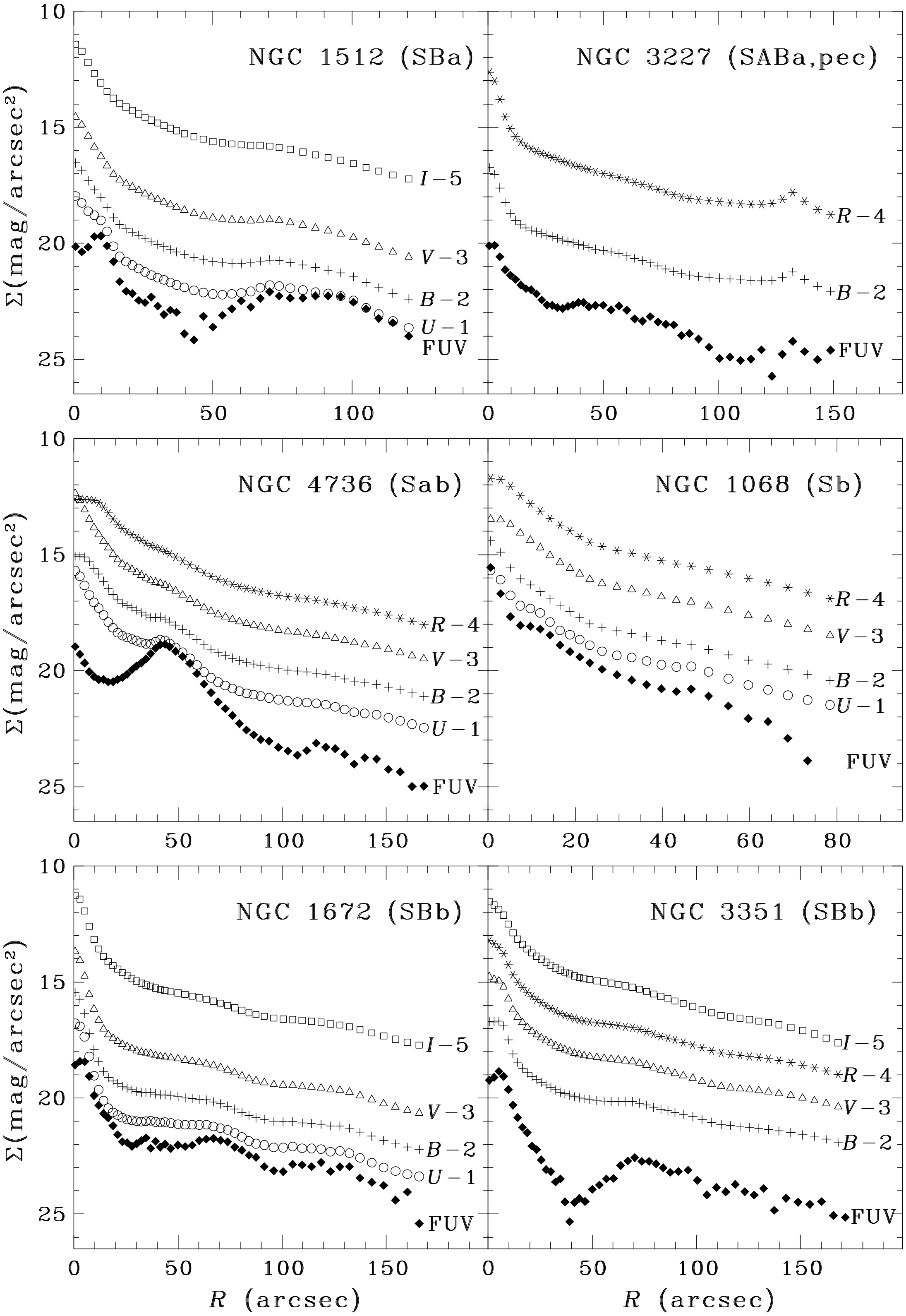

NGC 1512 (SBa)
NGC 3227 (SABa,pec)
NGC 4736 (Sab)
NGC 1068 (Sb)
NGC 1672 (SBb)
NGC 3351 (SBb)
Σ(mag/arcsec²)
R (arcsec)
I−5
V−3
B−2
U−1
R−4
FUV




Fig. 4b.—

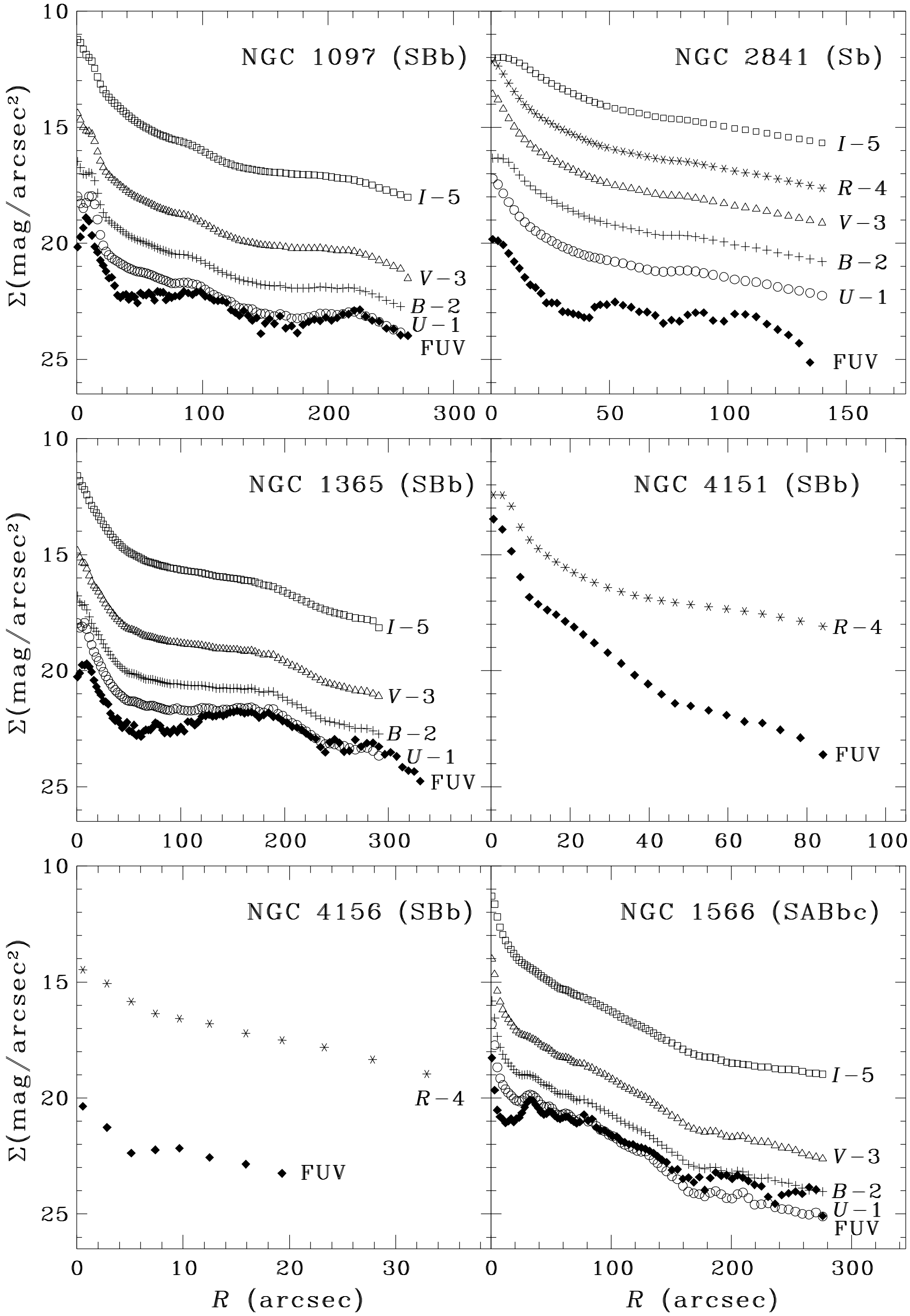

NGC 1097 (SBb)
NGC 2841 (Sb)
NGC 1365 (SBb)
NGC 4151 (SBb)
NGC 4156 (SBb)
NGC 1566 (SABbc)
Σ(mag/arcsec²)
R (arcsec)
I−5
R−4
V−3
B−2
U−1
FUV




Fig. 4c.—

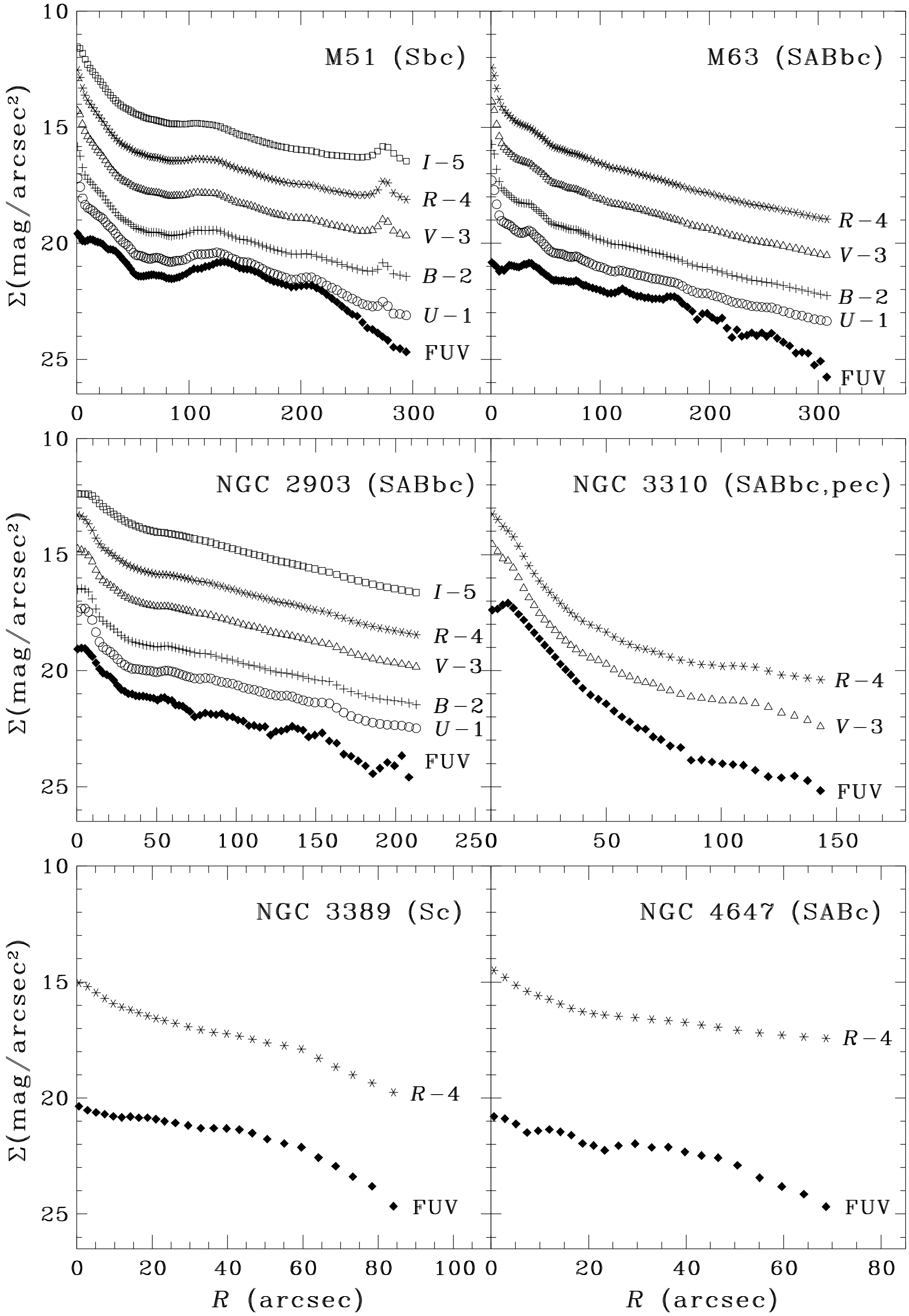
M51 (Sbc)
M63 (SABbc)
NGC 2903 (SABbc)
NGC 3310 (SABbc,pec)
NGC 3389 (Sc)
NGC 4647 (SABc)
I−5
R−4
V−3
B−2
U−1
FUV
Σ(mag/arcsec²)
R (arcsec)



Fig. 4d.—

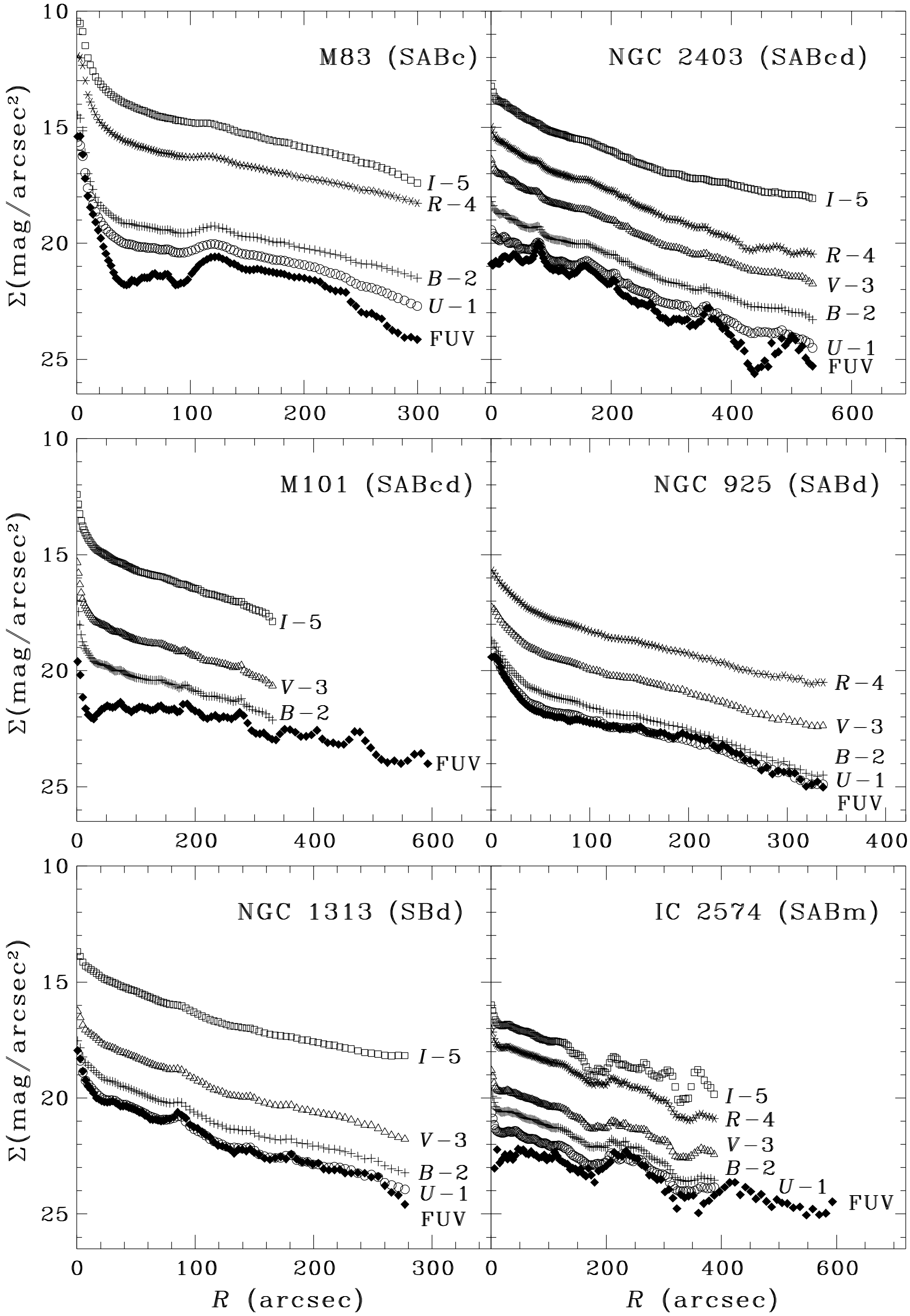

M83 (SABc)
NGC 2403 (SABcd)
M101 (SABcd)
NGC 925 (SABd)
NGC 1313 (SBd)
IC 2574 (SABm)
Σ(mag/arcsec²)
R (arcsec)
I−5
R−4
V−3
B−2
U−1
FUV




Fig. 4e.—

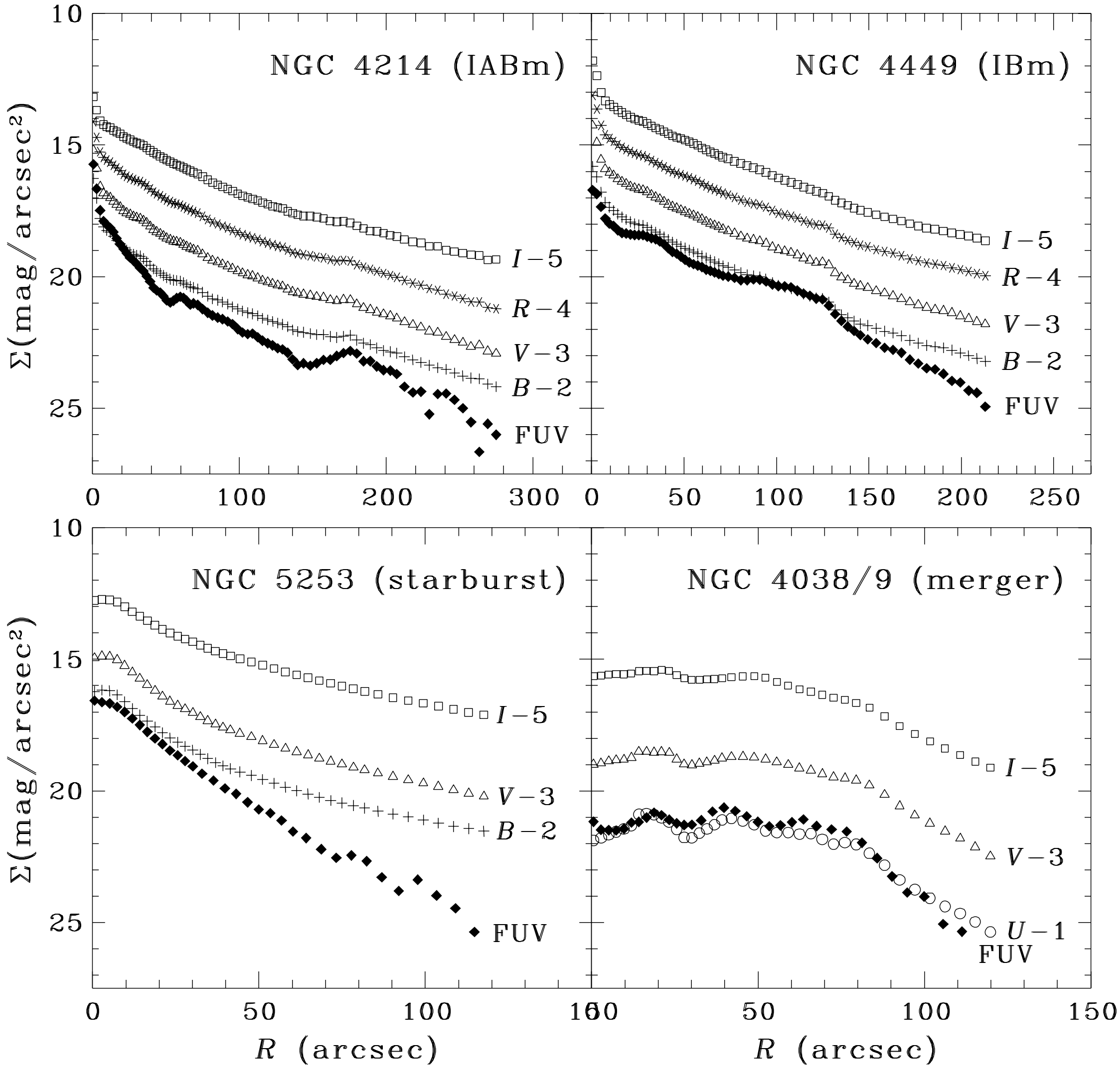
NGC 4214 (IABm)
NGC 4449 (IBm)
NGC 5253 (starburst)
NGC 4038/9 (merger)
Σ(mag/arcsec²)
R (arcsec)
I−5
R−4
V−3
B−2
U−1
FUV



Fig. 4f.—

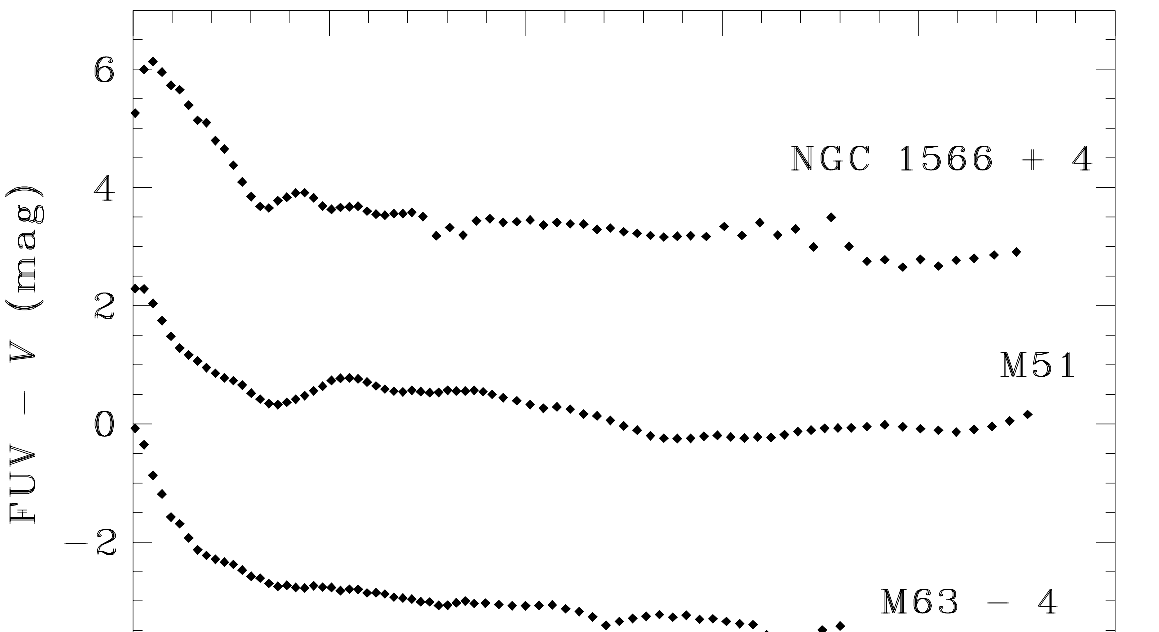

NGC 1566 + 4
M51
M63 − 4
FUV − V (mag)
R (arcsec)
6
4
2
0
−2
−4
0
50
100
150
200
250




Fig. 5.—

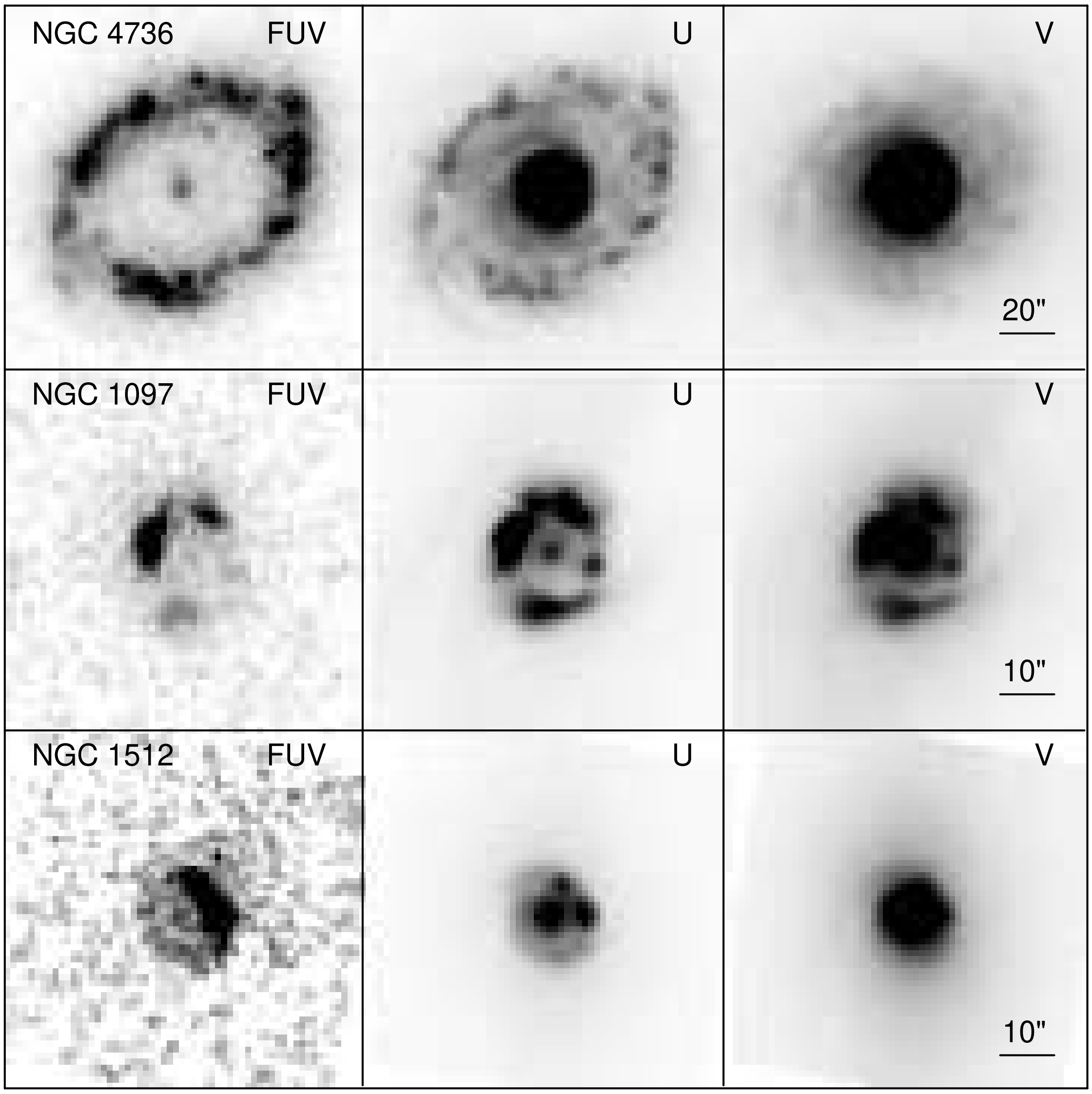


Fig. 6.—

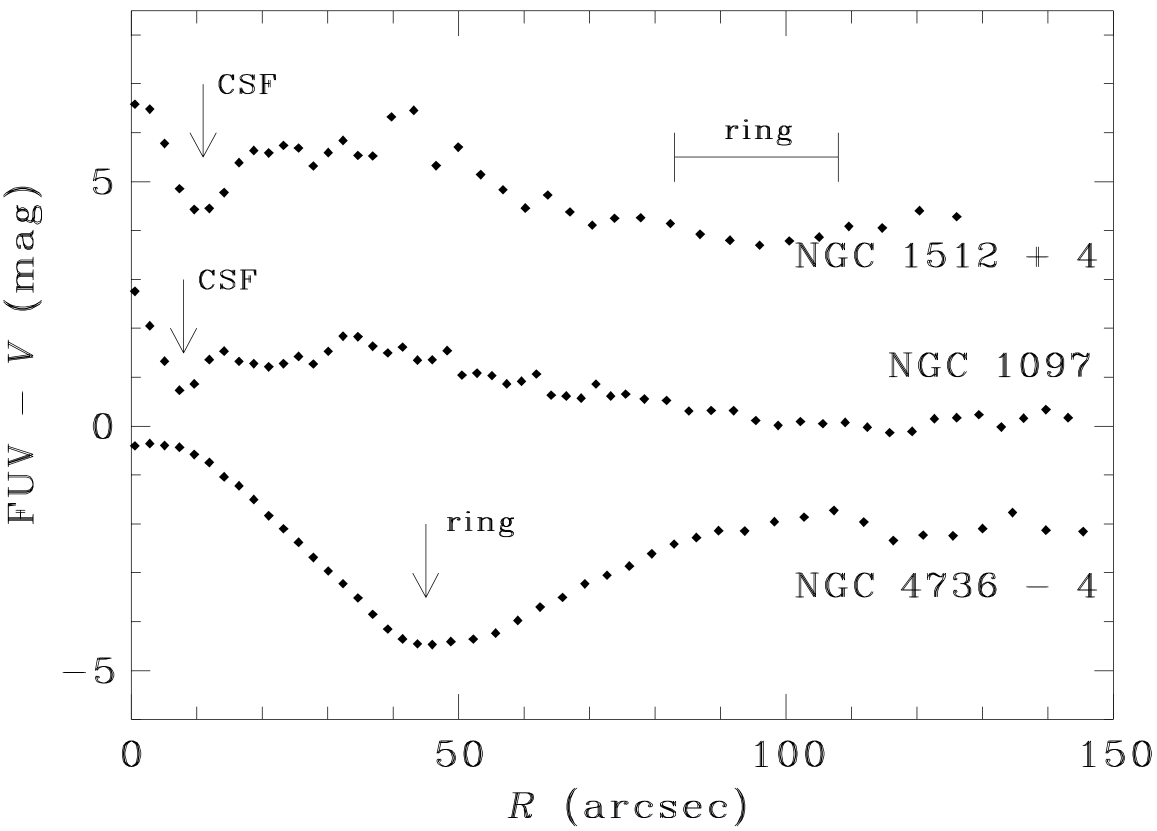
CSF
ring
NGC 1512 + 4
CSF
NGC 1097
ring
NGC 4736 − 4
FUV − V (mag)
R (arcsec)
5
0
−5
0
50
100
150



Fig. 7.—

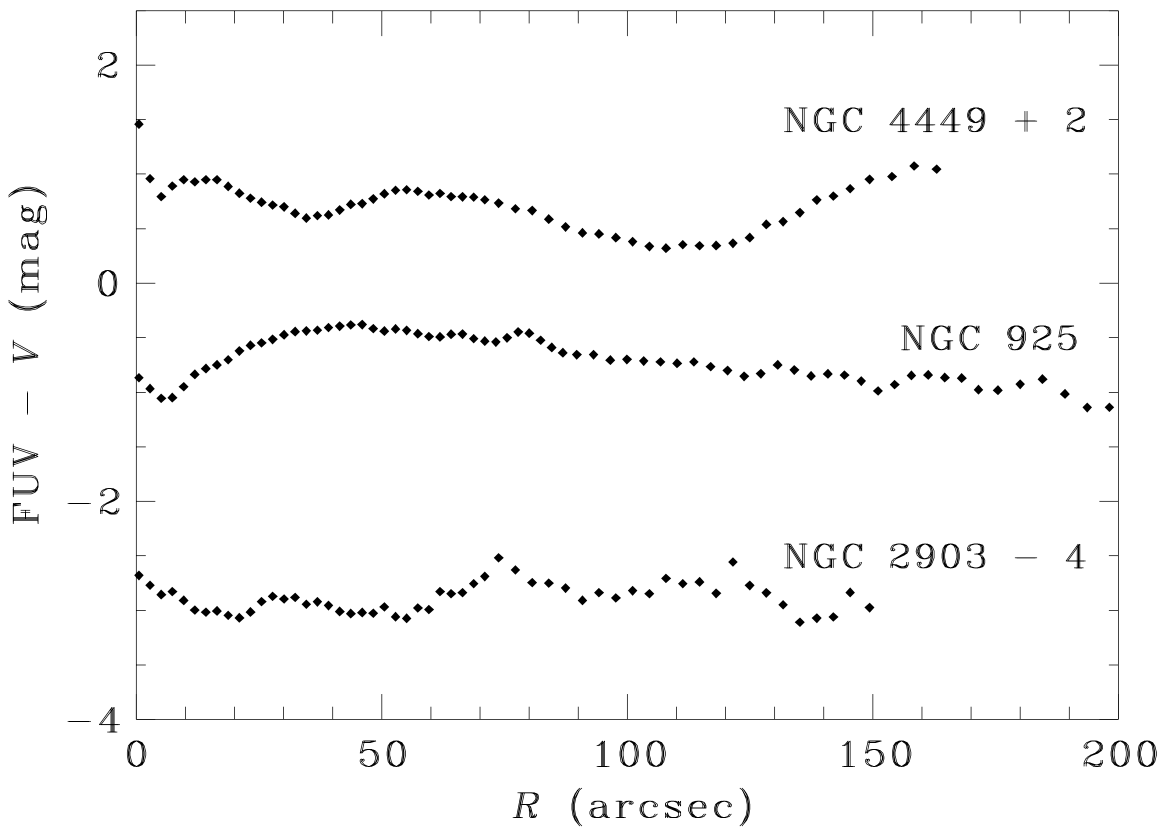

NGC 4449 + 2
NGC 925
NGC 2903 − 4
FUV − V (mag)
R (arcsec)
2
0
−2
−4
0
50
100
150
200




Fig. 8.—

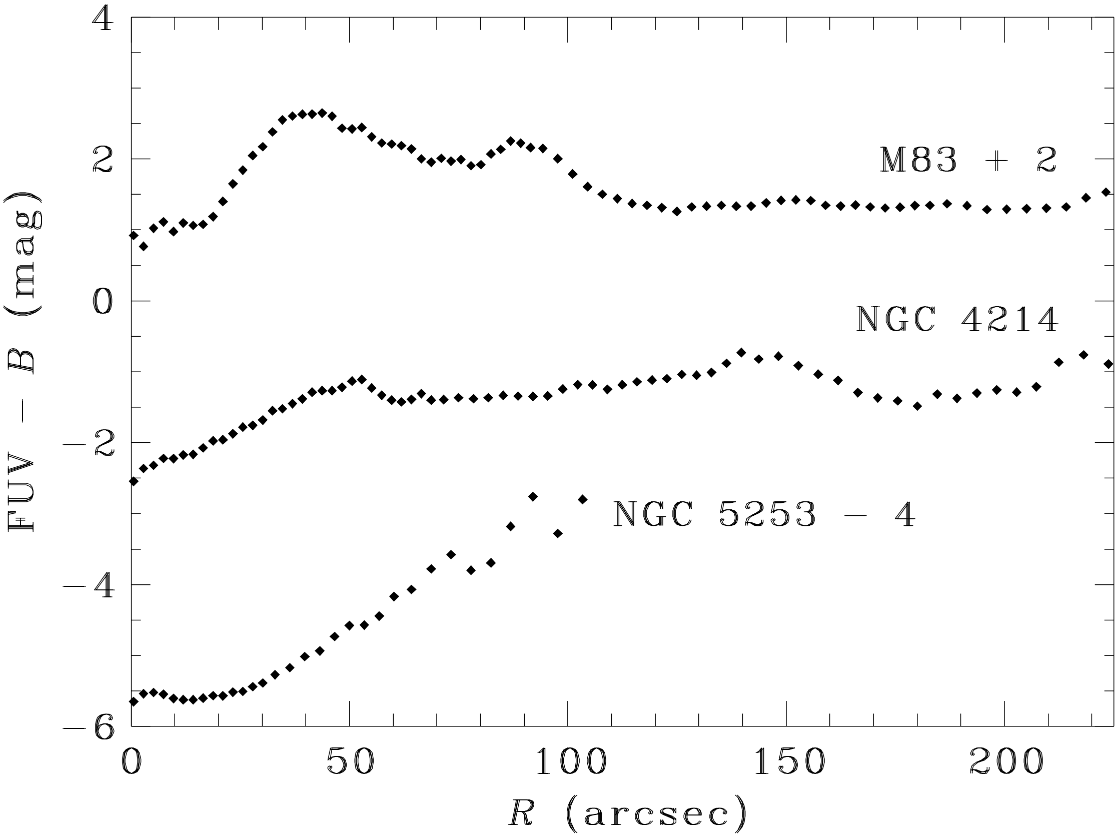
M83 + 2
NGC 4214
NGC 5253 − 4
FUV − B (mag)
R (arcsec)
4
2
0
−2
−4
−6
0
50
100
150
200



Fig. 9.—